Supporting Information for: Chirality-dependent dynamic evolution for trions in monolayer WS_2

Baixu Xiang,[†,‡,△] Renqi Wang,[†,△] Yuzhong Chen,[‡] Yubin Wang,[†,‡] Tingxiao Qin,[‡] Mengdi Zhang,[‡] Kenji Watanabe,[¶] Takashi Taniguchi,[¶] Wenhui Duan,[†,§,‖] Peizhe Tang,[⊥,#] Haiyun Liu,[‡] and Qihua Xiong[†,‡,‖,@]

†*State Key Laboratory of Low-Dimensional Quantum Physics and Department of Physics, Tsinghua University, Beijing,100084, P. R. China.*

‡*Beijing Academy of Quantum Information Sciences, Beijing 100193, P. R. China.*

¶*Advanced Materials Laboratory, National Institute for Materials Science, 1-1 Namiki, Tsukuba, 305-0044, Japan.*

§*Institute for Advanced Study, Tsinghua University, Beijing 100084, People's Republic of China.*

‖*Frontier Science Center for Quantum Information, Beijing, 100084, P. R. China.*

⊥*Materials Science and Engineering, Beihang University, Beijing 100191, P. R. China.*

#*Centerfor Free-Electron Laser Science, Max Planck Institute for the Structure and Dynamics of Matter, Hamburg 22761, Germany.*

@*Collaborative Innovation Center of Quantum Matter, Beijing, 100084, P.R. China.*

△*These authors contributed equally to this work.*

E-mail:

qihua_xiong@tsinghua.edu.cn.;peizhet@buaa.edu.cn; liuhy@baqis.ac.cn;

This PDF file includes:

Supplementary Note 1 to 11

Figure S1 to S15

Table S1,S2

Supporting Information Note 1: Sample preparation

Monolayer WS_2 and hexagonal boron nitride (h-BN) were mechanically exfoliated from bulk crystals using blue tape (Nitto) and scotch tape, respectively. The mechanically exfoliated monolayer WS_2 was identified by optical microscopy and characterized by Raman and PL spectroscopy. h-BN/WS_2/h-BN heterostructures were stacked on a fused quartz substrate using polyvinyl alcohol (PVA)-assisted transfer method. The samples were annealed after the transfer process under a vacuum (around 10^{-5} hPa) at 180°C for three hours and were placed in a liquid-helium cryostat for temperature-dependent experiments.

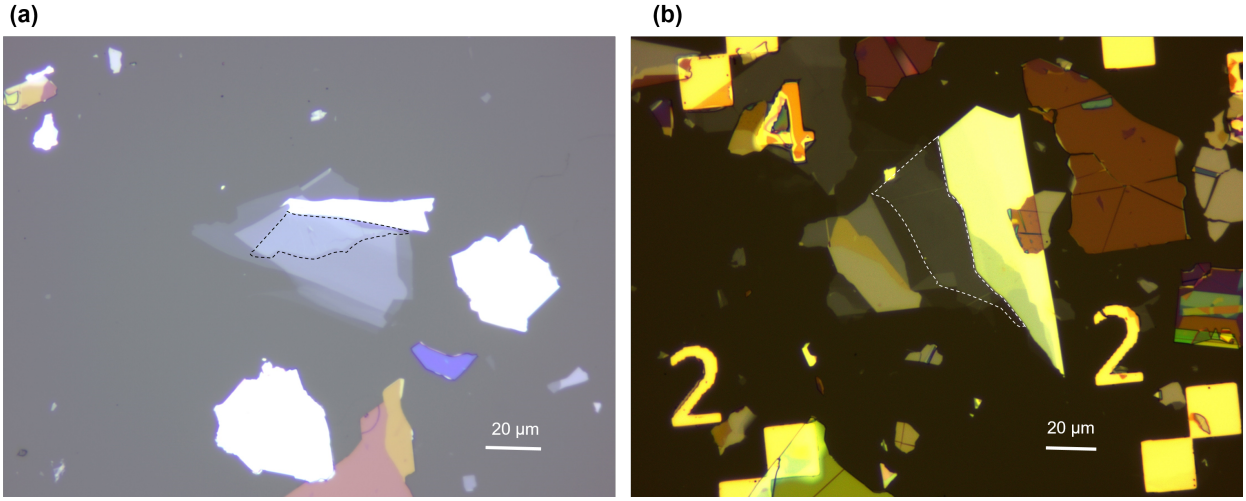

Figure S1: Optical microscope images of the samples 1 (a) and 2 (b). The black (white) dashed lines indicate the contours of the WS_2 layer of sample 1 (2). Scale bar, 20 μ m.

Supporting Information Note 2: Helicity-resolved ultrafast transient transmission spectroscopy and Dual-chopper methods

Helicity-resolved ultrafast transient transmission spectroscopy

The pump-probe experiments were performed in a transient absorption/transmission spectrometer (Helios fire from Ultrafast system). The infrared pulses (800 nm, 35 fs) were provided by a Ti: Sapphire amplifier (Coherent Inc.) working at 1 kHz repetition rate and split into two beams. One beam was sent into an optical parametric amplifier (OPA) to generate pump pulses with tunable photon energies, allowing resonant/near-resonant excitation of the samples. A set of long- and short-pass filters were used to cut the pump spectra with a full width at half maximum (FWHM) of about 40 meV. The probe pulses were white light continuum generated by focusing the other 800 nm laser beam into a sapphire plate and were delayed by a motorized delay line. The pump and probe beams were focused and overlapped on the sample surface, with 200 and 6 um spot sizes in diameter, respectively. A spectrometer equipped with a back-thinned CCD linear detector was used to detect the transmitted probe pulses. The pump-induced change $\frac{\Delta T}{T}=\frac{T_{on}-T_{off}}{T_{off}}$ was measured, where T_{on} and T_{off} represent the probe signals with the pump pulses on and off, respectively. We used two choppers to modulate the pump and probe lights separately to subtract scattered pump pulses, producing high data quality when the trion and exciton were resonantly excited. Besides, the polarization of each beam was independently controlled using broadband quarter-waveplates and linear polarizers.

Dual-chopper method

We use a dual-chopper on the path of the pump and probe beams to minimize the affection of the scattered pump light. As shown in Figure S1, pump and probe beams are triggered and choppered at half (500 Hz) and quarter frequency (250 Hz) of the laser repetition rate (1 kHz), respectively. In this configuration, the detection frequency is running at 1 kHz as well, acquiring four kinds of signals: $T_{on,on}$, $T_{off,on}$, $T_{on,off}$, and $T_{off,off}$. The first on(off) represents the state of the pump and the second one is the state of the probe light. Therefore, one obtains pure pump-on

signal $T_{on} = T_{on,on} - T_{on,off}$ by substracting the scattered pump ($T_{on,off}$), and pure pump-off signal $T_{off} = T_{off,on} - T_{off,off}$, in which $T_{off,off}$ is the ambient light.Then the differential transmission signals can be expressed by the following:

$$\frac{\Delta T}{T} = \frac{T_{on} - T_{off}}{T_{off}}$$

Thus, the scattered light of the pump light and the ambient light are effectively removed, allowing data collection under resonant conditions.

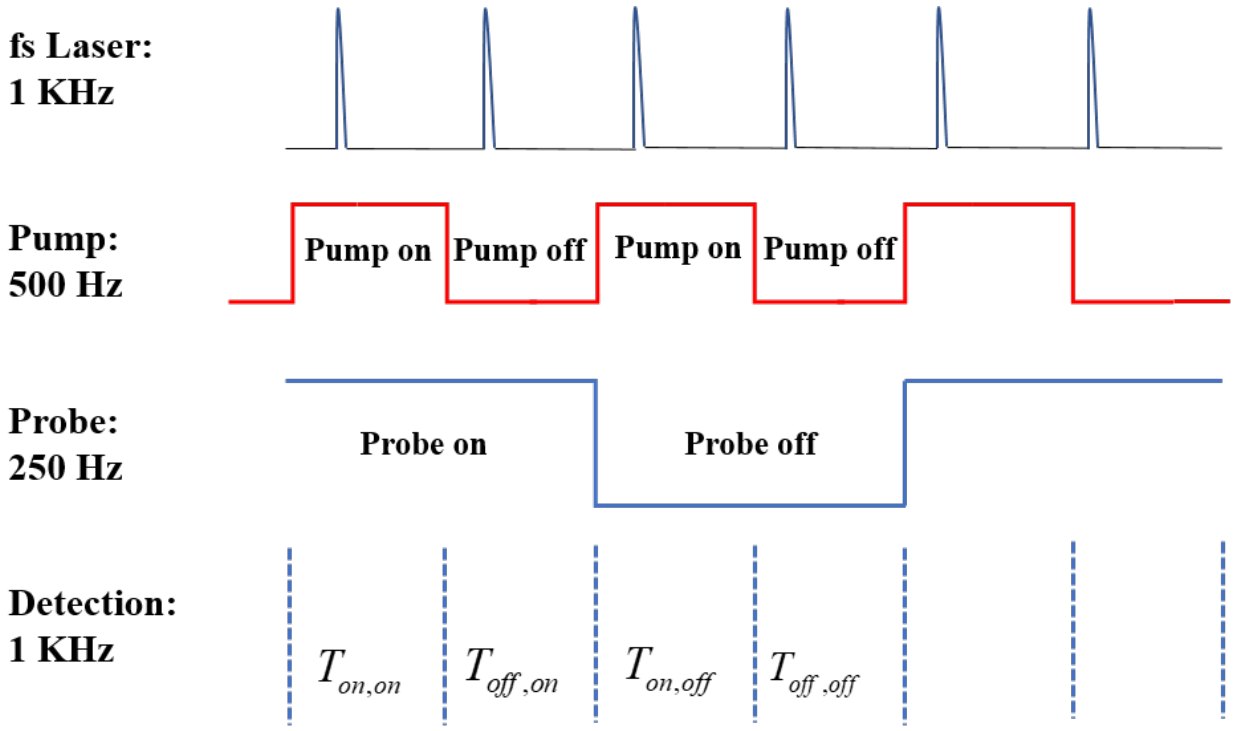

Figure S2: Schematic diagram of the dual-chopper modulation technique.

Supporting Information Note 3: Linear-response regime analysis for sample 1 and sample 2

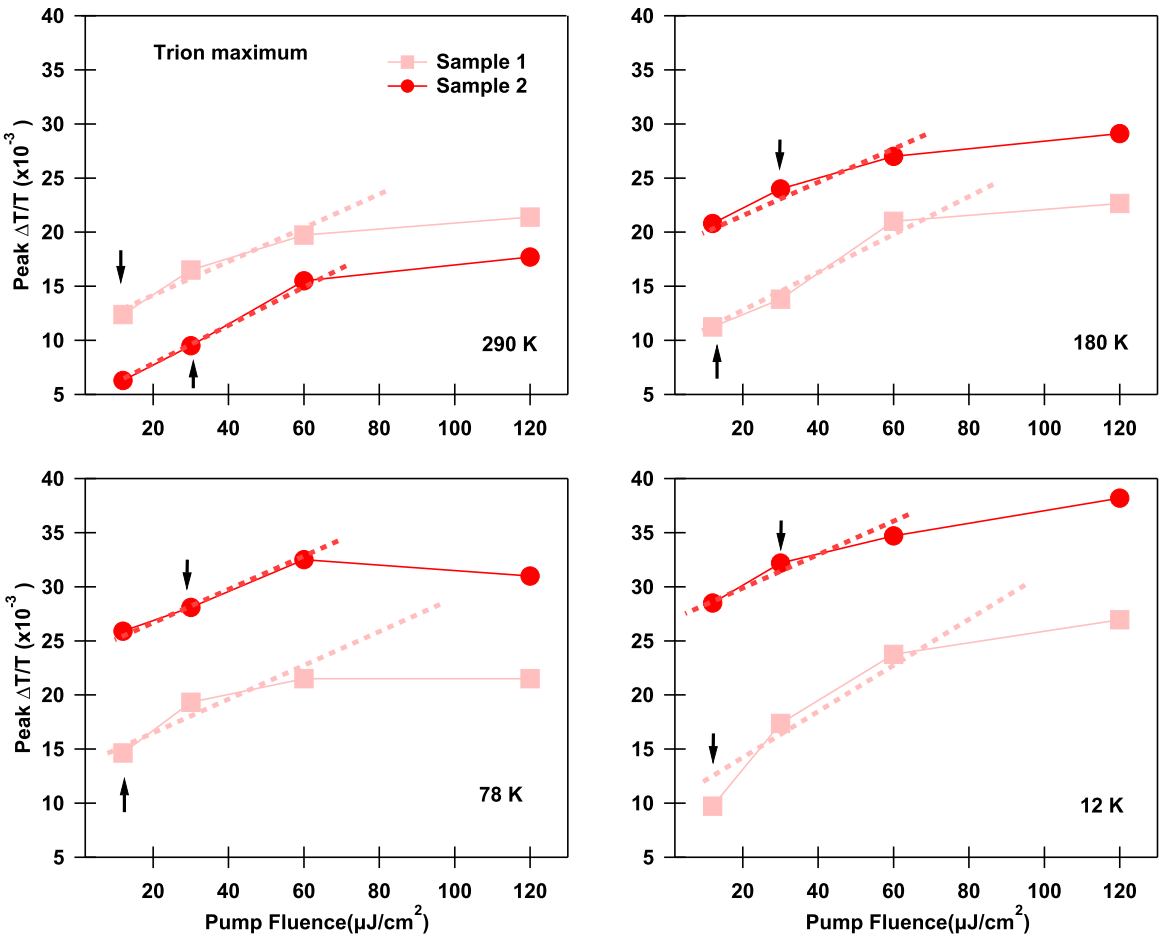

Figure S3: Pump fluence dependent of peak signals of trions for sample 1 and sample 2 at 290, 180, 78, and 12 K, respectively. The dashed lines are a guide to the eye to highlight the linear regime ($F < 60\ \mu\mathrm{J/cm^2}$) below saturation. Sample 1 and 2 were excited with a fluence at $F = 12$ and $30\ \mu\mathrm{J/cm^2}$, respectively, as marked by black arrows. Thus, we can conclude that the pump fluence below $30\ \mu\mathrm{J/cm^2}$ is in the linear-response regime for sample 1. The signals deviate from each other due to sample quality, optimizing conditions, etc.

Supporting Information Note 4: Time traces of $\frac{\Delta T}{T}$ extracted at the exciton resonance induced by different energy excitation

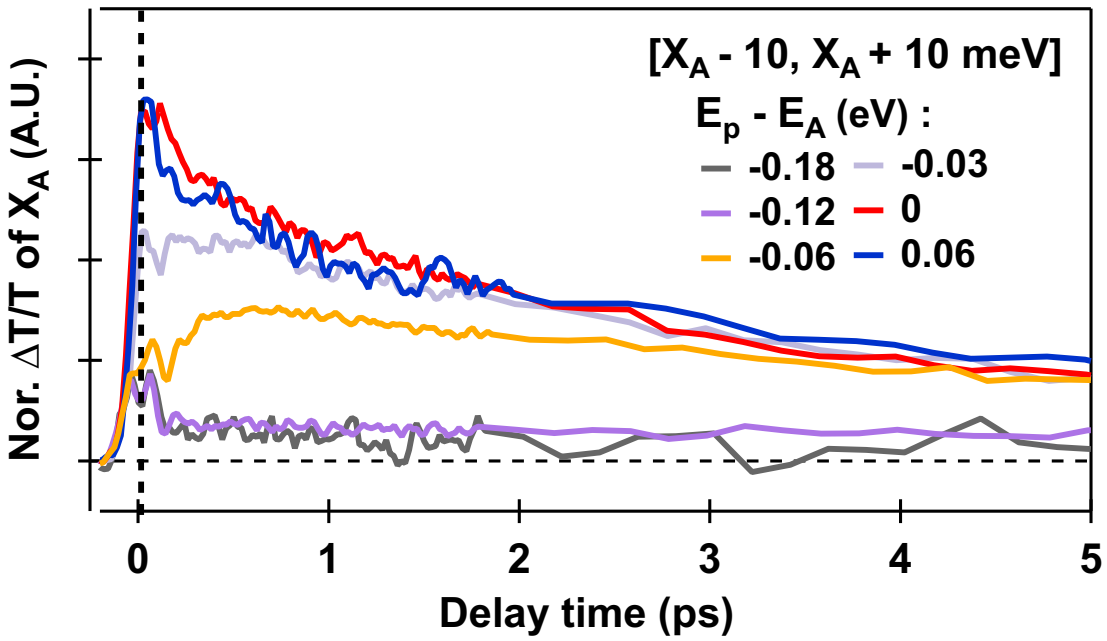

Figure S4: Dynamics integrated within a [-10, 10 meV] window around A-exciton, under different pump energies with the same pump fluence. $E_P - E_A = -0.06\ and\ 0$ eV correspond to resonant excitations of trion and A-exciton, respectively. Obviously, the resonant excitation of A-exciton is most efficient to generate A-exciton bleaching signal (red curve), which reaches its maximum around time-zero (marked by the dashed line) right after the pump excitation.

Supporting Information Note 5: Population recombination dynamics for sample 1 when resonantly pumping the A-exciton at room temperature

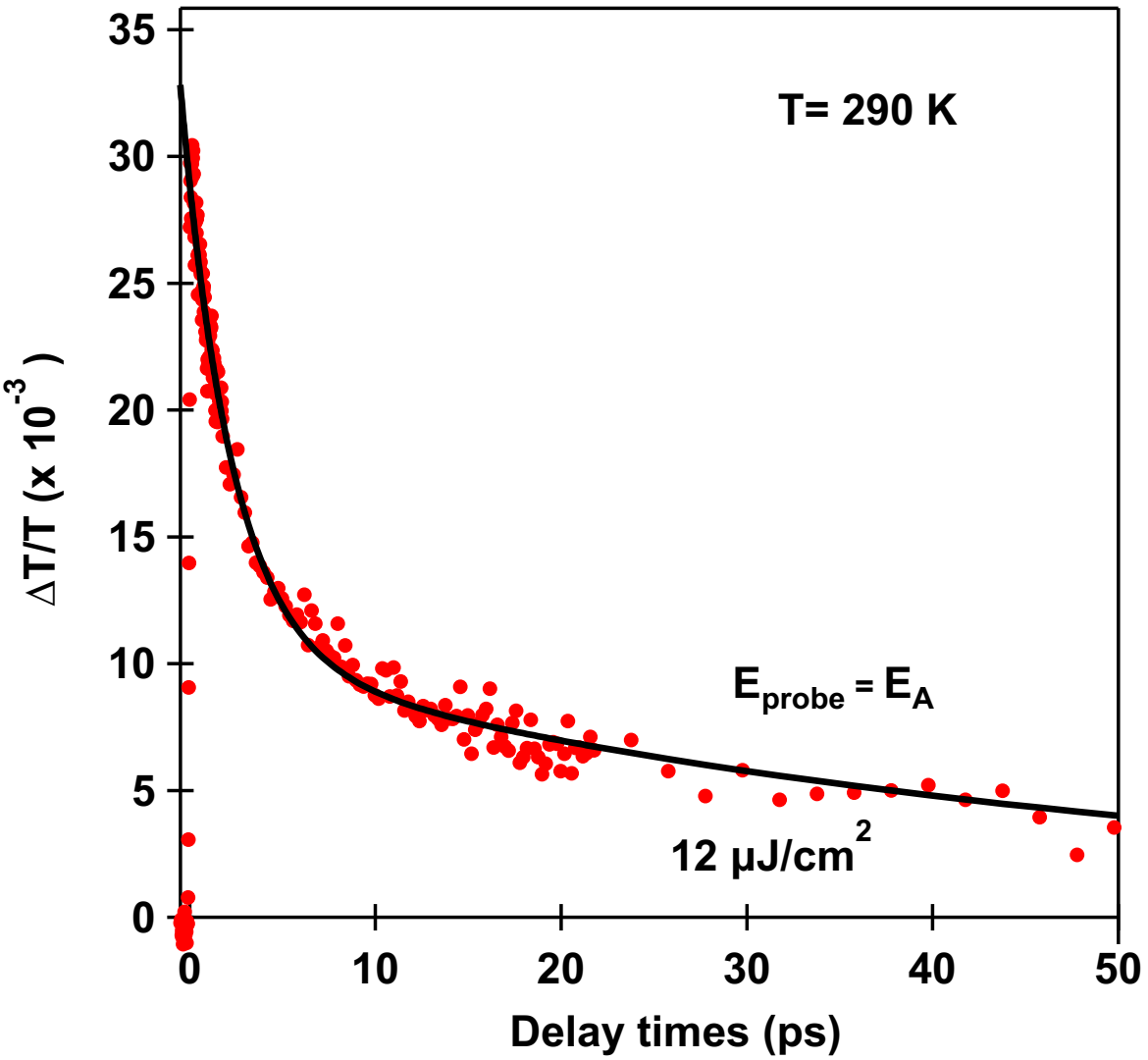

Figure S5: The decay dynamics of A-exciton($E_A = 2.00$ eV) exhibit a bi-exponential response. we attribute the fast decay τ_1 (2.7 ps) to the intrinsic radiative lifetime of A-exciton, while the slow decay τ_2 (49.3 ps) to the non-radiative lifetime, resulting from exciton-exciton scattering and exciton-phonon intra-valley scattering.[1]

Supporting Information Note 6: Spectroscopic characterization of monolayer WS_2(sample 2)

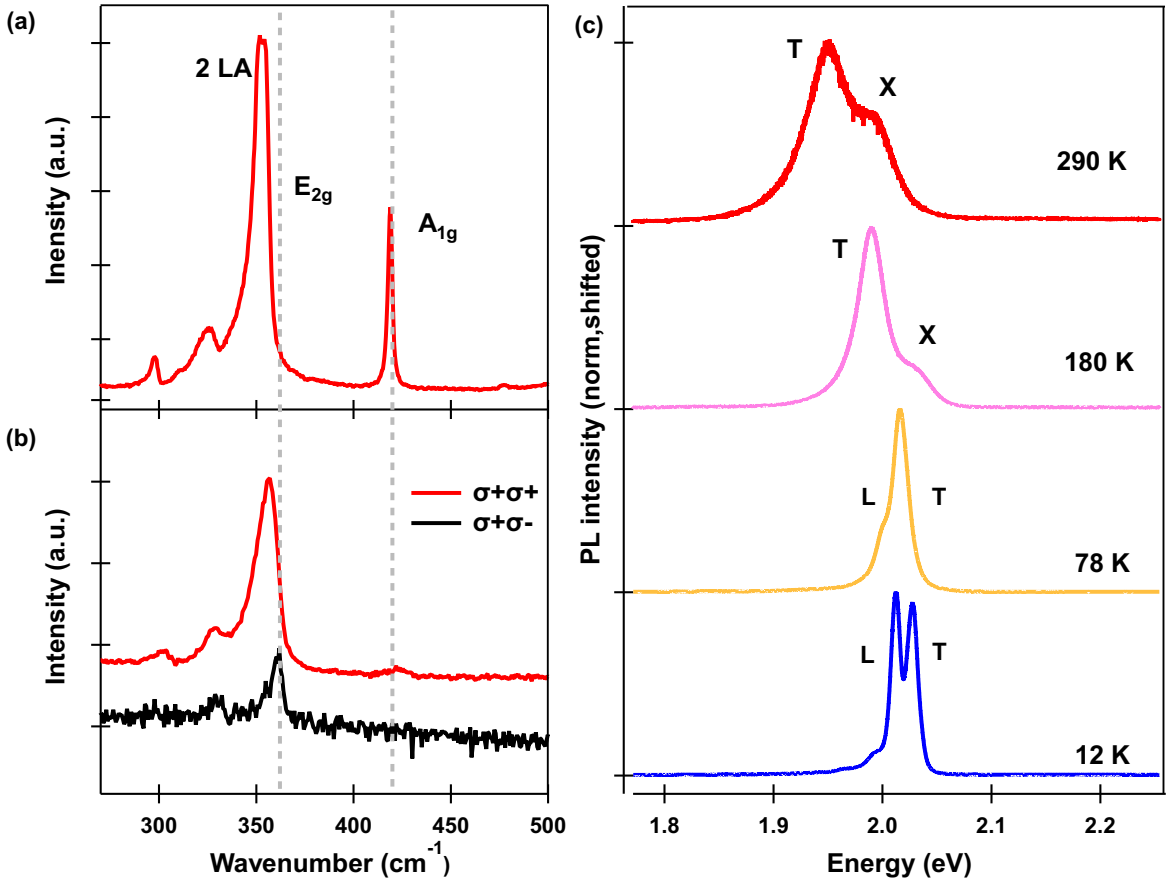

Figure S6: Raman and PL spectra of monolayer WS_2 (Sample 2). (a) Raman spectrum of h-BN/WS_2/h-BN sample 2 at room temperature, with an excitation laser wavelength of 514 nm and a power of 3 mW. In Raman spectroscopy, the A_{1g} and E_{2g} modes locate at 419 cm^{-1} (52 meV) and 359 cm^{-1}(44 meV), respectively (indicated by the dashed lines). The monolayer WS_2 can be determined from the Raman shift difference between the A_{1g} and E_{2g} lines. The strongest Raman peak at 352 cm^{-1} is ascribed to the second-order Raman mode 2 LA. (b) Polarization resolved Raman spectra with an excitation laser wavelength of 532 nm, the first order A_{1g} mode is only visible in the SCP configuration, while the E_{2g} mode is only observed in the OCP configuration. (c) Temperature evolution of PL spectra at a constant excitation power of 10 μW. At 290 and 180 K, the A-exciton (X) and trion (T) are well observed. As temperature decreases, the exciton and trion lines shift to higher energies (blue shift), and the relative peak strength of A-exciton decreases. At 78 and 12 K, the localized excitons (L) emerge, while the A-exciton disappears. These spectral features are consistent with previous results.[2,3]

Supporting Information Note 7: Pump spectra turned at trion resonance for each temperature in our measurements (sample 2)

.

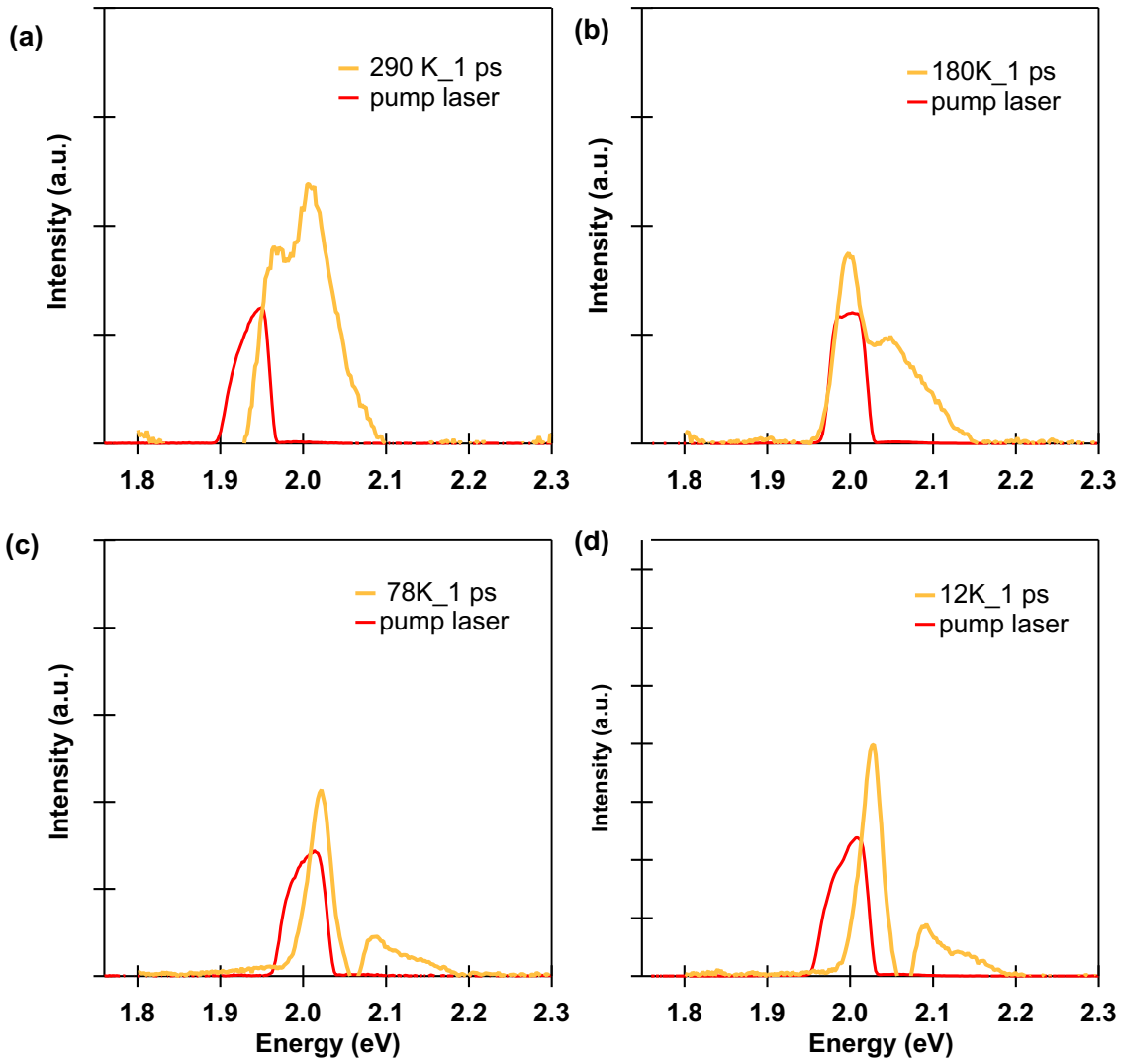

Figure S7: Pump spectra (red curves), together with differential transmission spectra of the h-BN/WS_2/h-BN sample2 for $\Delta t = 1$ ps at (a) 290 (b) 180 (c) 78 and (d) 12 K.

Supporting Information Note 8: Transient differential transmission spectra

Figure S7 shows the transient transmission spectra of monolayer WS_2 at the time delay of 1 ps in the SCP and OCP configurations. At 290 K, two significant ground state bleaching (GSB) features corresponding to trions and excitons dominate. The additional red-side negative differential transmission signal is attributed to the weak pump-induced absorption (PIA) features ($\Delta T/T < 0$), which stem from the formation of biexcitons.[4] In addition, with the temperature decreasing, the negative signals appearing between the trion and A-exciton in both SCP and OCP spectra at 78 K and 12 K may come from the energy blueshift of the trion, which is attributed to the inter-trion repulsive interaction.[5,6] It should be noted that trion triplets and singlets in our sample are pumped together due to their slight energy difference (about 15 meV illustrated in the PL spectrum in Figure S5 (c)), and they cannot be spectrally resolved in the transmission spectra. Nevertheless, our focus lies on the dynamics of trions and two types of trions resonantly created by pump light are natural in our sample.

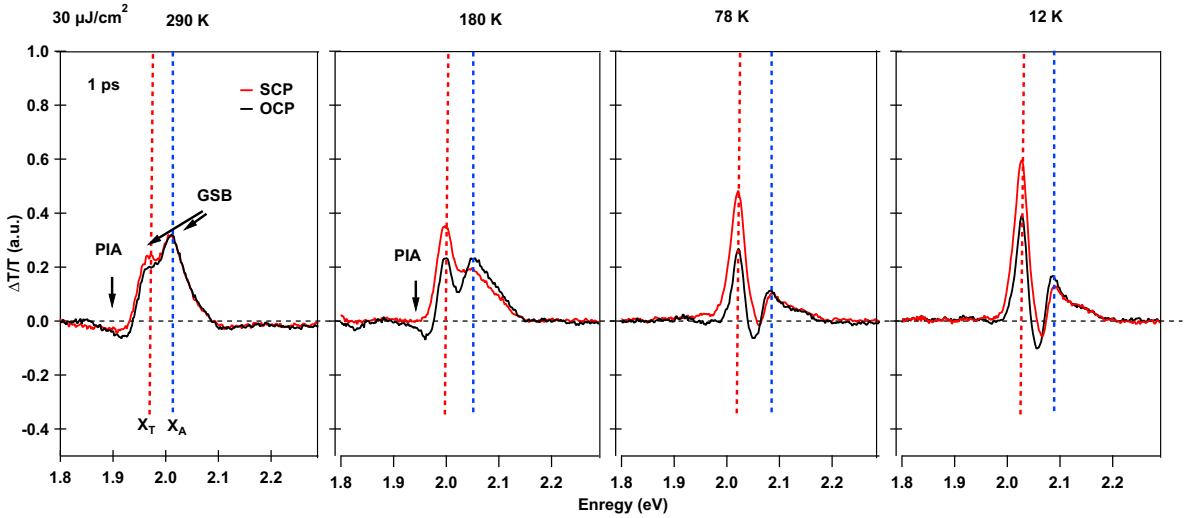

Figure S8: Transient transmission spectra of monolayer WS_2 at a time delay of 1 ps. PIA and GSB peaks are marked by black arrows in SCP (red lines) and OCP (black lines) spectra.

Supporting Information Note 9: Normalized decay curves of trions as a function of pump-probe delay time at different temperatures

We decompose the trion and exciton signals from the raw differential transmission spectra at different delay times. The spectral weight (i.e., the integrated area, I), which represents the population of excitons/trions, can be extracted by multiplying the peak amplitude (A) by the peak width (W). The populations of trions in the SCP configuration were normalized at the maximum value (Figure S6). Thus, the corresponding temporal evolutions of the trions and excitons populations are depicted in Figure 3e-h.

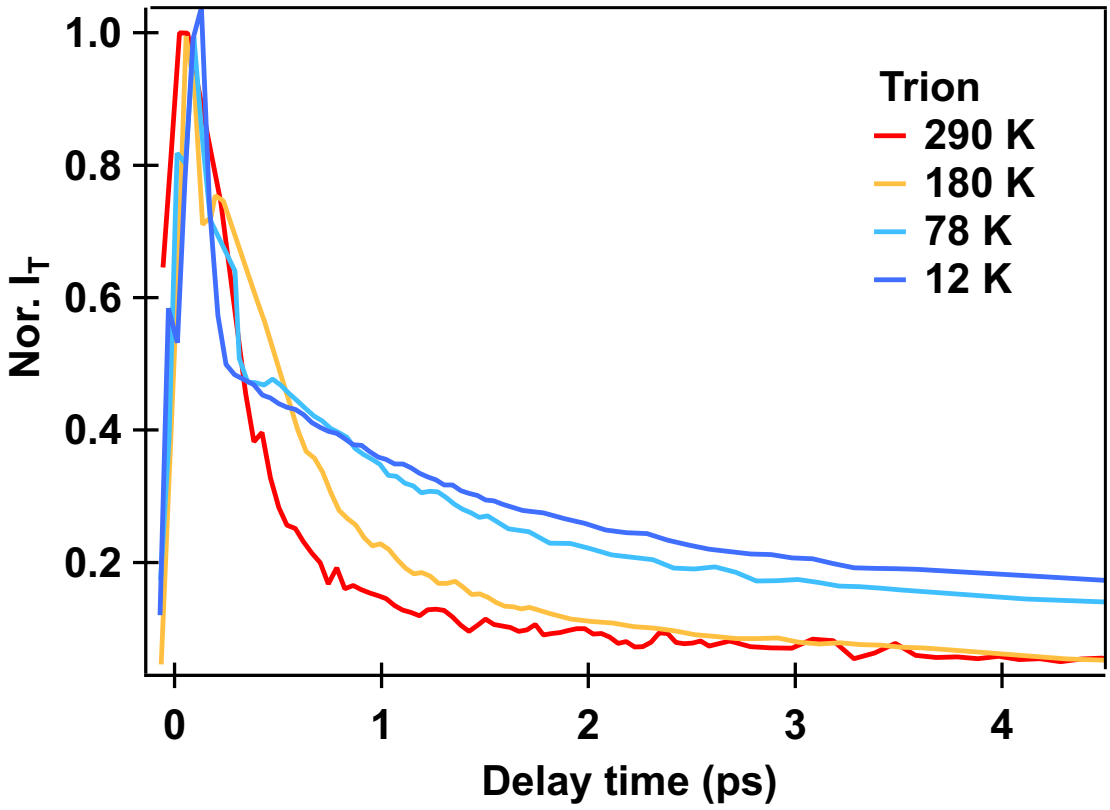

Figure S9: The temporal evolutions of trion population are normalized to the maximum value.

Supporting Information Note 10: Time traces of A-excitons and trions in the SCP and OCP configurations

As Figure S9 shows, the evolution behavior of X_A in the OCP configuration is similar to that of X_A at the pumped valley in the SCP configuration. Once X_T is initially pumped in one valley by CPL, two relaxation channels play the role of the emergency of X_A in the opposite unpumped valley. One is combined by the scattering processes ① and ② with a scattering time τ_1 (see Figure 1b in the main text), the pumped X_T transit to X_A at the same valley first, then relax to X_A at the opposite valley. This channel is much more efficient because the large population for X_A at the pumped valley has been observed in the SCP configuration (see Figure 2 and 3 in the main text). The other relaxation channel is combined by the scattering processes ③ and ④ with the scattering time τ_2 as shown in Figure 1b. The depolarization process for X_T between K and –K valleys occurs firstly, then the upconversion process changes the X_T at the unpumped valley to be X_A within the same valley. These two scattering channels are in parallel, thus the build-up time τ for the X_A observed in the OCP configuration should be $\tau{=}\tau_1\tau_2/(\tau_1+\tau_2)$, which is shorter than both τ_1 and τ_2 and is close to the build-up time of X_A at the pumped valley observed in the SCP configuration.

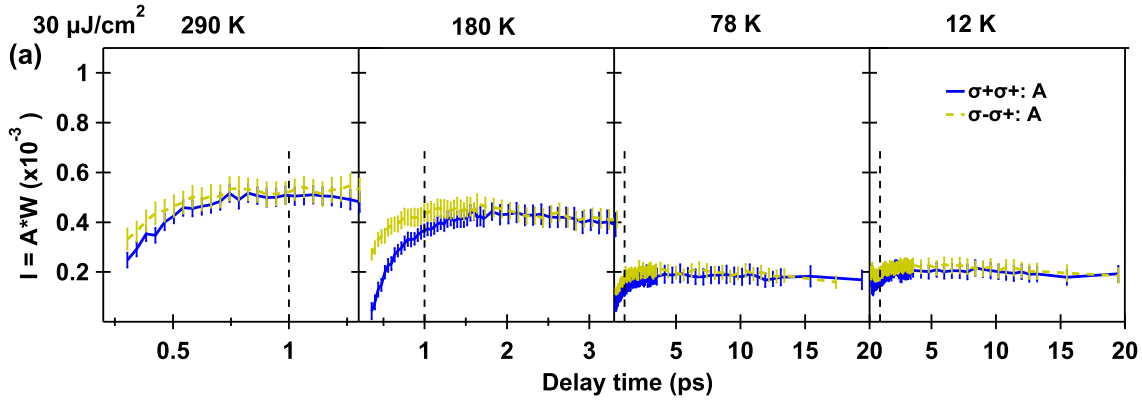

Figure S10: Due to off-resonance excitation for A-excitons, the exciton valley depolarization occurs rapidly compared to the trions.

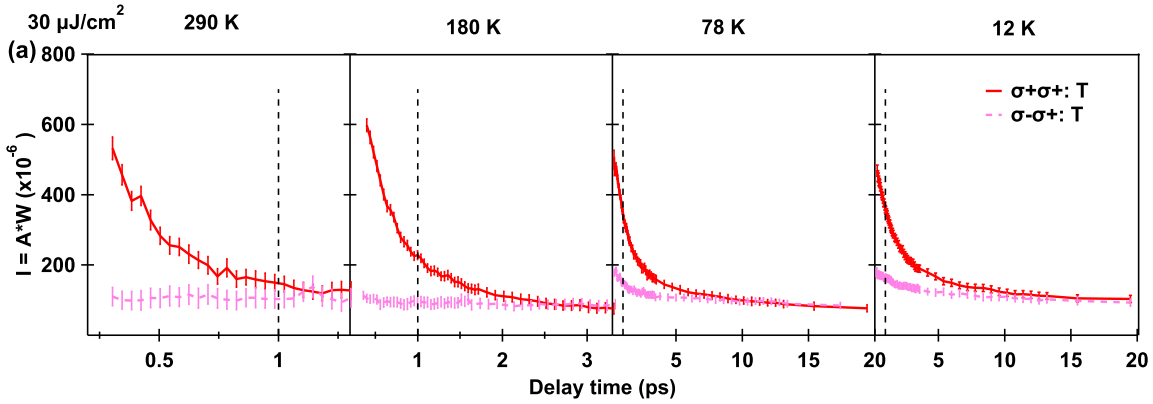

Figure S11: The population of trions in the SCP reaches equivalent at approximately 1 ps, and prolongs to longer time with the temperature decreasing, owing to the phonon-assisted intervalley scattering mechanism.

Supporting Information Note 11: Theoretical calculation

We present a Boltzmann equation model that comprehensively incorporates trion-exciton scattering[2,7] and intervalley depolarization processes, primarily driven by Coulomb exchange interactions[8,9] and dark-exciton mediated exciton-phonon scattering,[10,11] as illustrated in the main text. This model aims to accurately replicate the fundamental characteristics observed in OCP and SCP configurations in the pump-probe experiments conducted at different temperatures.

The investigation of the temporal evolution of trions and excitons employed semiconductor Bloch equations (SBEs).[12] SBEs are widely recognized for their applicability in describing both coherent and non-coherent quantum kinetics. The simulation results presented in the main text predominantly focus on non-coherent processes and were computed through the Boltzmann equations derived from SBEs.

The phonon-induced interplay between trions and excitons, crucial within the framework of the Boltzmann equations, can be formally expressed as $\langle T_{tr}|\hat{H}_{e-ph}|X\rangle$ according to Fermi's golden rule. Here, the el-ph Hamiltonian, as well as the trion and exciton wavefunctions, are required. To calculate the exciton and trion wavefunctions, we utilize electron and hole wavefunctions obtained from the $\mathbf{k}\cdot\mathbf{p}$ model for transition metal dichalcogenides (TMDs)[13,14] as the basis. The parameters for the model were fitted from first-principle calculations of the monolayer WS_2 band structure, carried out using the Vienna Ab initio Simulation Package (VASP).[15–17] While sophisticated techniques such as diffusion Monte Carlo (DMC)[17] and the Stochastic Variational Method[18] have been developed to determine the ground state binding energy and wavefunctions for trions and excitons, this study employs effective mass approximations and a variational method with the variational form proposed in prior research.[19–21] We calculated the phonon dispersion and electron-phonon coupling strength using the Quantum Espresso package[22] and EPW.[23] These results provide the electron-phonon interaction Hamiltonian and justify considering only the A_{1g} phonon in the trion-exciton scattering channel.

In addition to the intravalley trion-exciton channel, we also consider the intervalley channel. However, the scattering rates for the intervalley depolarization of excitons and trions are introduced

as phenomenological parameters in the model, and these can be compared with experiments and previous theoretical work.[11,24–30]

Comprehensive details are presented following for reference, providing nuanced insights into our numerical methodology.

Exciton and trion wavefunctions

The effective $\mathbf{k}\cdot\mathbf{p}$ model for $\mathrm{WX_2}$ ($\mathrm{W}=\mathrm{Mo,\ W}$ and$\mathrm{X}=\mathrm{S,\ Se}$) near the K and -K points, accounting for the effects of spin-orbit coupling (SOC),[12,13] can be formulated as:

$$\hat{H}=\hbar v(\tau k_x\hat{\sigma}_x+k_y\hat{\sigma}_y)+\frac{E_{bg}}{2}\hat{\sigma}_z-\Delta_{VB}\tau\frac{\hat{\sigma}_z-1}{2}\hat{s}_z \tag{1}$$

where v is the Fermi velocity, E_{bg} stands for the band gap between the conduction and valence bands at the K and -K points, τ represents the valley degree of freedom, and $\hat{\sigma}$ and $\hat{s}_z$ correspond to the Pauli matrices linked with the orbital and spin degrees of freedom, respectively. The spin splitting in the valence band, represented by Δ_{VB}, is a result of spin-orbit coupling (SOC). These parameters in the model Hamiltonian are typically determined through fitting with results from the first-principles calculations. As an example, $2\Delta_{VB}=0.43$ eV and $\hbar v=4.38$ eV·Å are obtained for $\mathrm{WS_2}$.[15–17]

Then, we calculate the electronic band structure based on the effective $\mathbf{k}\cdot\mathbf{p}$ model to get eigenstates for conduction band (CB) edge and valence band (VB) edge $\epsilon_{\tau,c(v)}(\mathbf{k})$ and their Bloch wavefunctions near different valleys ($\tau=\pm$K), which can serve as the basis to construct wavefunctions for excitons and trions. Furthermore, given the parabolic band dispersion near the band edge, we get the effective masses for electrons (m_e) in CB and for holes (m_h) in VB, and the masses for the exciton and negatively charged trion, denoted as M_X and M_T respectively, are the sum of the electron and hole effective masses, expressed as m_e+m_h and $2m_e+m_h$.

To accurately describe bound states like excitons and trions and obtain their binding energy, the Coulomb interactions between electron-hole (e-h) are taken into account in the Bethe-Salpeter

equation (BSE)[31–33] which typically encompasses both the Hartree and exchange terms. However, for simplicity, we will consider only the Hartree term initially, which primarily contributes to the binding of electrons and holes. We first express the creation operators for excitons in valley τ with momentum $\mathbf{Q}_X$ in the basis of Bloch wavefunctions of the electron and hole at the band edges,[34] then we have:

$$\hat{X}^{\dagger}_{\tau,\mathbf{Q}_X} = \frac{1}{\sqrt{A}} \sum_{\mathbf{k}} \psi_{\tau,\mathbf{Q}_X}(\mathbf{k}) \hat{c}^{\dagger}_{\tau,\mathbf{k}+\lambda_e\mathbf{Q}_X,s(\tau)} \hat{b}_{\tau,\mathbf{k}-\lambda_h\mathbf{Q}_X,s(\tau)} \tag{2}$$

Herein $\psi_{\tau,\mathbf{Q}_X}(\mathbf{k})$ is the exciton wavefunction which will be used for the calculation of the scattering strength discussed in the following. $\hat{c}_{\tau,\mathbf{k}}$ and $\hat{b}_{\tau,\mathbf{k}}$ represents electron annihilation operators with wave vector $\mathbf{k}$ in CB and VB near τ valley. A is the quantized area and $\lambda_{e(h)} = \frac{m_{e(h)}}{M_X} = \frac{m_{e(h)}}{m_e+m_h}$.

After a basis transformation of the exciton wavefunctions for the electron Bloch wavefunctions near K(-K) points $\psi_{\tau,\mathbf{Q}_X}(\mathbf{k}) = \phi_{\tau,\mathbf{Q}_X}(\mathbf{k}) \exp(i(\tau\varphi_{\mathbf{k}+\lambda_e\mathbf{Q}_X} + \tau\varphi_{\mathbf{k}-\lambda_h\mathbf{Q}_X})/2)$ (where $\varphi_{\mathbf{k}}$ is the phase of wave vector $\mathbf{k}$), we could further simplify the form factor $\langle u_{c\mathbf{k}+\mathbf{q}}|u_{c\mathbf{k}}\rangle\langle u_{v\mathbf{k}'-\mathbf{q}}|u_{v\mathbf{k}'}\rangle$ within the BSE and obtain the Wannier equations.[34,35]

$$\begin{aligned}\left[\epsilon_{\tau,c}(\mathbf{k}+\lambda_e\mathbf{Q}_X) - \epsilon_{\tau,v}(\mathbf{k}-\lambda_h\mathbf{Q}_X)\right]\phi_{\tau,\mathbf{Q}_X}(\mathbf{k}) - \frac{1}{A}\sum_{\mathbf{q}} V_{2D}(\mathbf{q})\phi_{\tau,\mathbf{Q}_X}(\mathbf{k}-\mathbf{q}) \\ = E_{\tau,X}(\mathbf{Q}_X)\phi_{\tau,\mathbf{Q}_X}(\mathbf{k})\end{aligned} \tag{3}$$

Herein, $\varepsilon_{\tau,c}(\mathbf{k})$ and $\varepsilon_{\tau,v}(\mathbf{k})$ in the left-hand represent eigen-energy for CB and VB edges obtained from $\mathbf{k}\cdot\mathbf{p}$ model. $V_{2D}(\mathbf{q}) = \frac{e^2}{\varepsilon}\frac{2\pi}{q(1+qr_0)}$ is the Rytova-Keldysh potential which is widely used in 2D materials considering the Coulomb screening.[36–38] In this equation, ε denotes the average permittivity of the environment, and r_0 is the screening length. Its real space form can be obtained through Fourier transformation as $V_{2D}(\mathbf{r}) = \frac{\pi e^2}{\varepsilon r_0}[H_0(\frac{r}{r_0}) - Y_0(\frac{r}{r_0})]$, with H_0 representing the Struve function and Y_0 as the second kind Bessel function.[36,38,39]

Accordingly, we do the Fourier transformation for the exciton wavefunctions to real space

$$\Psi_{X,\tau,\mathbf{Q}_X}(\mathbf{R},\mathbf{r}) = \frac{1}{\sqrt{A}} e^{-i\mathbf{Q}_X\cdot\mathbf{R}}\phi_{\tau,\mathbf{Q}_X}(\mathbf{r}) = \frac{1}{\sqrt{A}} e^{-i\mathbf{Q}_X\cdot\mathbf{R}} \frac{1}{(2\pi)^2}\int d\mathbf{k}\phi_{\tau,\mathbf{Q}_X}(\mathbf{k}) e^{i\mathbf{k}\cdot\mathbf{r}}$$

and obtain the hydrogen-like Schrödinger equations within the effective mass approximation[39]

$$\left[-\frac{\hbar^2\nabla^2_{\mathbf{R}}}{2M_X}-\frac{\hbar^2\nabla^2_{\mathbf{r}}}{2\mu}-V_{2D}(\mathbf{r})\right]\Psi_{X,\tau,\mathbf{Q}_X}(\mathbf{R},\mathbf{r})=\left(\frac{h^2\mathbf{Q}_X^2}{2M_X}-E_{b,X}\right)\Psi_{X,\tau,\mathbf{Q}_X}(\mathbf{R},\mathbf{r}) \tag{4}$$

where the $E_{b,X}$ represents the exciton binding energy, and it is related to $E_{\tau,X}(\mathbf{Q}_X)$ in Eq. 3 by $E_{\tau,X}(\mathbf{Q}_X)=E_{bg}-E_{b,\tau,X}+\frac{h^2\mathbf{Q}_X^2}{2M_X}$.

Similarly, the trion operator in valley τ with momentum $\mathbf{Q}_T$ can also be written in an electronic basis. Taking the triplet trion defined in the main text as an example and defining $\eta_{e(h)}=\frac{m_{e(h)}}{M_T}=\frac{m_{e(h)}}{2m_e+m_h}$:

$$\begin{aligned}&\hat{T}^\dagger_{\tau,\mathbf{Q}_T}|FS\rangle=\\&\frac{1}{A}\sum_{\mathbf{k_1},\mathbf{k_2}}\psi_{\tau,\mathbf{Q}_T}(\mathbf{k_1},\mathbf{k_2})\hat{c}^\dagger_{-\tau,\mathbf{k_1}+\eta_e\mathbf{Q}_T,s(\tau)}c^\dagger_{\tau,\mathbf{k_2}+\eta_e\mathbf{Q}_T,s(\tau)}\hat{b}_{\tau,\mathbf{k_1}+\mathbf{k_2}-\eta_h\mathbf{Q}_T,s(\tau)}\hat{c}_{-\tau,\mathbf{Q}_T,s(\tau)}|FS\rangle\end{aligned} \tag{5}$$

Where the $\psi_{\tau,\mathbf{Q}_T}(\mathbf{k_1},\mathbf{k_2})$ is the trion wavefunctions in the reciprocal space, and $|FS\rangle$ represents the ground state with the VB fully occupied and the lowest CB partially occupied.[34] The corresponding equations of trion wavefunctions in the real space in the effective mass approximation have been derived as

$$\begin{aligned}[-&\frac{\hbar^2\nabla^2_{\mathbf{R}}}{2M_T}-\frac{\hbar^2\nabla^2_{\mathbf{r_1}}}{2\mu}-\frac{\hbar^2\nabla^2_{\mathbf{r_2}}}{2\mu}-\frac{\hbar^2\nabla_{\mathbf{r_1}}\cdot\nabla_{\mathbf{r_2}}}{2m_h}-V_{2D}(\mathbf{r_1})-V_{2D}(\mathbf{r_2})\\&+V_{2D}(|\mathbf{r_1}-\mathbf{r_2}|)]\Psi_{T,\tau,\mathbf{Q}_T}(\mathbf{R},\mathbf{r_1},\mathbf{r_2})=\left(\frac{h^2\mathbf{Q}_T^2}{2M_T}-E_{b,T}\right)\Psi_{T,\tau,\mathbf{Q}_T}(\mathbf{R},\mathbf{r_1},\mathbf{r_2})\end{aligned} \tag{6}$$

In this equation, the $E_{b,T}$ is the trion binding energy with $E_T=E_{bg}-E_{b,T}+\frac{h^2\mathbf{Q}_T^2}{2M_T}$ and we have used the relations

$$\begin{aligned}\Psi_{T,\tau,\mathbf{Q}_T}(\mathbf{R},\mathbf{r_1},\mathbf{r_2})&=\frac{1}{\sqrt{A}}e^{-i\mathbf{Q}_T\cdot\mathbf{R}}\phi_{\tau,\mathbf{Q}_T}(\mathbf{r_1},\mathbf{r_2})\\&=\frac{1}{\sqrt{A}}e^{-i\mathbf{Q}_T\cdot\mathbf{R}}\frac{1}{(2\pi)^4}\int d\mathbf{k_1}d\mathbf{k_2}\phi_{\tau,\mathbf{Q}_T}(\mathbf{k_1},\mathbf{k_2})e^{i\mathbf{k_1}\cdot\mathbf{r_1}+i\mathbf{k_2}\cdot\mathbf{r_2}}\end{aligned} \tag{7}$$

$$\psi_{\tau,\mathbf{Q}_T}(\mathbf{k_1},\mathbf{k_2})=\phi_{\tau,\mathbf{Q}_T}(\mathbf{k_1},\mathbf{k_2})\exp(i(-\tau\varphi_{\mathbf{k_1}+\eta_e\mathbf{Q}_T}+\tau\varphi_{\mathbf{k_2}+\eta_e\mathbf{Q}_T}+\tau\varphi_{\mathbf{k_1}+\mathbf{k_2}-\eta_h\mathbf{Q}_T})/2)$$

.

We solve these equations mentioned above (Eqs. 3 and 6) numerically to obtain the binding energies and wavefunctions of neutral and charged excitons. For trions, we utilize variational methods to bypass the direct solution of these equations and separate wavefunctions into components about center-of-mass motion and relative motion. Variational expressions, as previously suggested in the literature [see details in Refs.[19,21,40]], are utilized to describe the relative motion part of wavefunctions, where a, b, c are the variational parameters of the unit of length.

$$\begin{aligned} \phi_{\tau,\mathbf{Q}_X}(\mathbf{r}; a) &\propto \exp(-r/a) \\ \phi_{\tau,\mathbf{Q}_T}(\mathbf{r_1}, \mathbf{r_2}; \{b, c\}) &\propto (\exp(-r1/b - r2/c) + \exp(-r1/c - r2/b) \end{aligned} \tag{8}$$

Using the following parameters: $m_e = m_h = 0.32\, m_e$, $r_0 = 38$ Å and $\varepsilon = \varepsilon_0$,[41,42] the variational parameters that minimize the exciton and trion energy functional are found to be $a = 12.9$ Å, $b = 12.8$ Å, and $c = 32.1$ Å. The corresponding binding energies are $E_{b,X} = 0.5$ eV and $E_{b,T} = 25$ meV. These results are in quantitative agreement with experimental data and prior theoretical predictions.[41]

The first-principle calculations of electron-phonon coupling

To investigate the phonon-assisted upconversion rate from intravalley trions to excitons, we need to consider the electron-phonon (el-ph) coupling strength for the lowest CB near the K and -K valleys assisted by the phonon mode with the energy of $\hbar\omega_{\nu,\mathbf{Q}}$, denoted as $|g_{cc,\nu}(\mathrm{K}, \mathbf{Q})|$. In this study, we employed the Quantum Espresso coupled with EPW code to compute the phonon dispersion and el-ph coupling matrix.[22,23,43] Based on the calculated phonon dispersion as shown in Fig. S13(a), we find that the energies of A_2' (ZO_1), $\mathrm{A}_{1\mathrm{g}}$ (HP) and E' ($\mathrm{LO}_2, \mathrm{TO}_2$) phonon modes are similar to trion binding energy. Consequently, we focus on these phonon modes and reveal that the el-ph coupling strength associated with the $\mathrm{A}_{1\mathrm{g}}$ (HP) mode near the band edge is significantly larger compared to the other modes [see Fig. S13(b)].

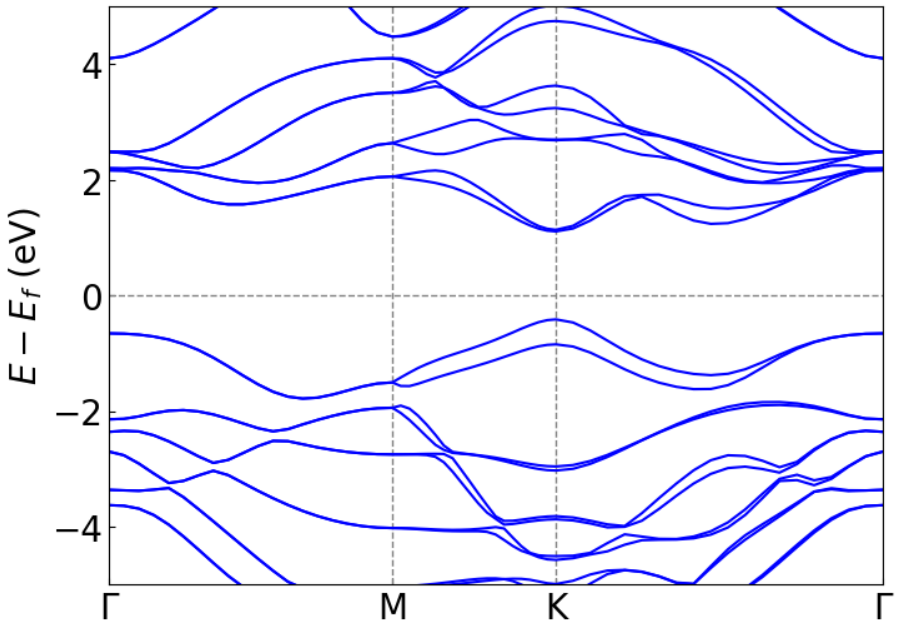

Figure S12: Electronic band structure calculations for WS_2 were performed using first-principles methods. The parameters for the $\mathbf{k} \cdot \mathbf{p}$ model can be derived from this band structure.

We calculate the el-ph coupling matrix linked to the A_{1g} mode systemically as shown in Fig. S13(c) and observe its maximum absolute value (approximately 350 meV·Å) at the Γ point within the phonon Brillouin zone (BZ), consistent with previous findings.[44] This absolute value exhibits isotropic decay as the momentum increases. For simplicity, we approximate this isotropic decay behavior fitted with a Gaussian function and use it in the following simulations.

The phonon-assisted upconversion rate

The el-ph interaction allows the coupling between excitons and negatively charged trions in the K valley. The Hamiltonian considering el-ph interaction is shown in Eq. 9 near the -K valley, which relates with the K valley by time-reversal symmetry. The operators $\hat{c}^{\dagger}_{-K,\mathbf{k},\uparrow}$ and $\hat{a}_{\mathbf{Q}}$ are electron and phonon operators respectively. We represent the el-ph coupling strength as $g_{\mathbf{Q}}$ which is a simplified form of $g_{cc,\mathrm{A_{1g}}}(-\mathrm{K}, \mathbf{Q})$ shown above.

$$\hat{H}_{el-ph} = \frac{1}{\sqrt{A}} \sum_{\mathbf{k},\mathbf{Q}} g_{\mathbf{Q}} \hat{c}^{\dagger}_{-\mathrm{K},\mathbf{k}+\mathbf{Q},\uparrow} \hat{c}_{-\mathrm{K},\mathbf{k},\uparrow} (\hat{a}_{\mathbf{Q}} + \hat{a}^{\dagger}_{-\mathbf{Q}}) \tag{9}$$

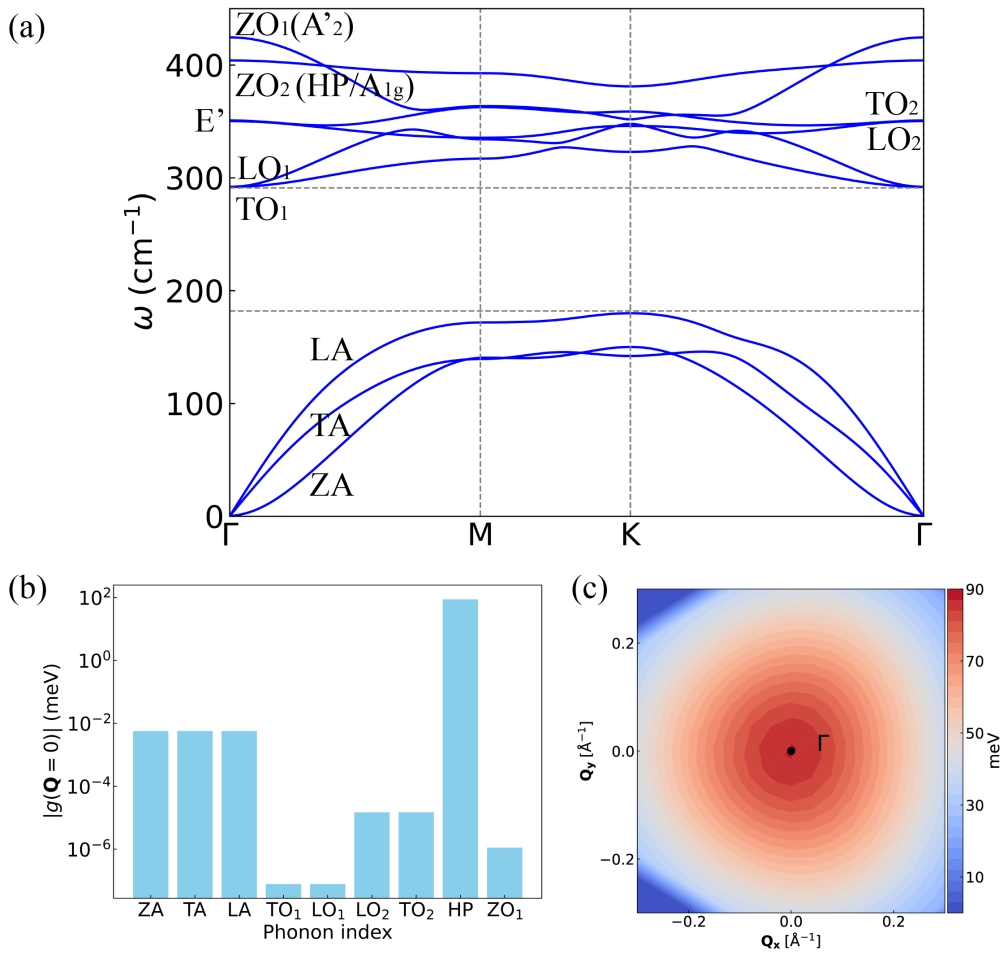

Figure S13: (a) The phonon dispersion of monolayer WS_2. In the figure, each phonon mode has been systematically labeled, wherein the nearly dispersionless ZO_2 mode is the out-of-plane vibration mode, also referred to as the homopolar (HP) or A_{1g} mode.[45] (b) The electron-phonon coupling matrix for the lowest conduction band is obtained from first-principles calculations, considering each phonon mode with wave vectors $\mathbf{Q} = 0$. The diagram is plotted in logarithmic coordinates. (c) The electron-phonon coupling matrix for HP mode near the Γ point. Specific details can be found in Supplementary Material (SM) Section 11.2.

Specifically, excitons can capture an additional free electron from the conduction band to create a trion while emitting a phonon to conserve energy and momentum. Conversely, lower-energy trions can be scattered into excitons by absorbing a phonon, resulting in the excitation of a free electron in the conduction band. Therefore, the coupling between trions $|T_{\mathbf{Q}_T}, 1\rangle = T^{\dagger}_{\mathbf{Q}_T}|FS\rangle \otimes |1\rangle_{ph}$ (herein $|n\rangle_{ph}$ is the Fock state with phonon number n and see the notion of $|FS\rangle$ in Eq. 5) and excitons with additional electrons in CB edge $\hat{c}^{\dagger}_{\mathbf{k+q},\uparrow}\hat{c}_{\mathbf{k},\uparrow}|X_{\mathbf{Q}_X}, 0\rangle_{ph} = \hat{c}^{\dagger}_{\mathbf{k+q},\uparrow}\hat{c}_{\mathbf{k},\uparrow}X^{\dagger}_{\mathbf{Q}_X}|FS\rangle \otimes |0\rangle_{ph}$ can be calculated as follows:

$$\begin{aligned}\langle X_{\mathbf{Q}_X}, 0|\hat{c}^{\dagger}_{\mathbf{k},\uparrow}\hat{c}_{\mathbf{k+q},\uparrow}\hat{H}_{e-ph}|T_{\mathbf{Q}_t}, 1\rangle = \frac{1}{A^2}\sum_{\mathbf{k_1}}\psi^*(\mathbf{k_1} + \eta_e\mathbf{Q}_T - \lambda_e\mathbf{Q}_X)g_{\mathbf{q}+\mathbf{Q}_X} \\ \psi(\mathbf{k_1}, (1-\eta_e)\mathbf{Q}_T - \mathbf{Q}_X)\sum_{\mathbf{k_2}}\langle FS|\hat{c}^{\dagger}_{\mathbf{k},\uparrow}\hat{c}_{\mathbf{k+q},\uparrow}\hat{c}^{\dagger}_{\mathbf{k_2+q+Q}_X,\uparrow}\hat{c}_{\mathbf{k_2},\uparrow}\hat{c}^{\dagger}_{\mathbf{Q}_T-\mathbf{Q}_X,\uparrow}\hat{c}_{\mathbf{Q}_T,\uparrow}|FS\rangle\end{aligned} \tag{10}$$

Herein, $\psi(\mathbf{k})$ and $\psi(\mathbf{k_1}, \mathbf{k_2})$ are exciton and trion wavefunctions defined in the previous section, with the subscript of valley index and center-of-mass being disregarded. In this work, we mainly focus on the case with $\mathbf{Q}_X = \mathbf{Q}_T = 0$, the scattering rate of the phonon-assisted upconversion process is approximated as follows:

$$G_{\mathbf{k},\mathbf{q}} = \langle X, 0|\hat{c}^{\dagger}_{\mathbf{k},\uparrow}\hat{c}_{\mathbf{k+q},\uparrow}\hat{H}_{e-ph}|T, 1\rangle = \frac{1}{A^2}\sum_{\mathbf{k_1}}\psi^*(\mathbf{k_1})g_{\mathbf{q}}\psi(\mathbf{k_1}, \mathbf{0})f_{\mathbf{k}}(1 - f_{\mathbf{k+q}}) \tag{11}$$

where $f_{\mathbf{k}}$ represents the Fermi-Dirac distribution of the electron state in the lowest conduction band with wave vector $\mathbf{k}$.

Boltzmann equation

We apply the Boltzmann equations to simulate the dynamic evolution of pumped trions and compare it with the experimental results. Some approximations are used here, including the factorization of N-electron density matrices[14,46] and the Markov approximation.[14,47] Once we have determined the trion-exciton coupling strength discussed above, the related Hamiltonian in a sin-

gle valley has the form as follows:

$$\begin{aligned}\hat{H}_0 =& E_T\hat{T}^\dagger\hat{T} + E_X\hat{X}^\dagger\hat{X} + \sum_{\mathbf{k}}\epsilon_{\mathbf{k}}\hat{c}^\dagger_{\mathbf{k}}\hat{c}_{\mathbf{k}} + \sum_{\mathbf{q}}\hbar\omega_0\hat{a}^\dagger_{\mathbf{q}}\hat{a}_{\mathbf{q}} \\ \hat{H}_{LO} =& \sum_{\mathbf{k},\mathbf{q}}\{G_{\mathbf{q}}\hat{X}^\dagger\hat{T}\hat{c}^\dagger_{\mathbf{k}+\mathbf{q}}\hat{c}_{\mathbf{k}}\hat{a}_{\mathbf{q}} + G^*_{\mathbf{q}}\hat{a}^\dagger_{\mathbf{q}}\hat{c}^\dagger_{\mathbf{k}}\hat{c}_{\mathbf{k}+\mathbf{q}}\hat{T}^\dagger\hat{X}\}\end{aligned} \tag{12}$$

Herein, $\hat{T}$ and $\hat{X}$ are trion and exciton operators with zero wave vectors and the E_T and R_X are corresponding quasiparticle energies (we drop the momentum subscript index for brevity). The third and fourth terms in the first line represent the electron and phonon Hamiltonian introduced above. The second line $\hat{H}_{LO}$ is the trion-exciton scattering Hamiltonian and $G_{\mathbf{q}} \approx G_{\mathbf{k},\mathbf{q}}$ is the approximated trion-exciton coupling matrix (see Eq. 11). The evolution of the particle number of trions and excitons can be described by semiconductor Bloch equations[14]

$$\begin{aligned}i\hbar\frac{d}{dt}\langle\hat{T}^\dagger\hat{T}\rangle =& -i\hbar\frac{d}{dt}\langle\hat{X}^\dagger\hat{X}\rangle = \langle[\hat{T}^\dagger\hat{T}, \hat{H}_0 + \hat{H}_{LO}]\rangle \\ =& \sum_{\mathbf{k},\mathbf{q}}\{-G_{\mathbf{q}}\langle\hat{X}^\dagger\hat{T}\hat{c}^\dagger_{\mathbf{k}+\mathbf{q}}\hat{c}_{\mathbf{k}}\hat{a}_{\mathbf{q}}\rangle + G^*_{\mathbf{q}}\langle\hat{a}^\dagger_{\mathbf{q}}\hat{c}^\dagger_{\mathbf{k}}\hat{c}_{\mathbf{k}+\mathbf{q}}\hat{T}^\dagger\hat{X}\rangle\}\end{aligned} \tag{13}$$

$$\begin{aligned}i\hbar\frac{d}{dt}\langle\hat{X}^\dagger\hat{T}\hat{c}^\dagger_{\mathbf{k}+\mathbf{q}}\hat{c}_{\mathbf{k}}\hat{a}_{\mathbf{q}}\rangle|_0 =& \langle[\hat{X}^\dagger\hat{T}\hat{c}^\dagger_{\mathbf{k}+\mathbf{q}}\hat{c}_{\mathbf{k}}\hat{a}_{\mathbf{q}}, \hat{H}_0]\rangle \\ =& -(E_X - E_T + \epsilon_{\mathbf{k}+\mathbf{q}} - \epsilon_{\mathbf{k}} - \hbar\omega_0)\langle\hat{X}^\dagger\hat{T}\hat{c}^\dagger_{\mathbf{k}+\mathbf{q}}\hat{c}_{\mathbf{k}}\hat{a}_{\mathbf{q}}\rangle\end{aligned} \tag{14}$$

$$\begin{aligned}i\hbar\frac{d}{dt}\langle\hat{X}^\dagger\hat{T}\hat{c}^\dagger_{\mathbf{k}+\mathbf{q}}\hat{c}_{\mathbf{k}}\hat{a}_{\mathbf{q}}\rangle|_{LO} =& \langle[\hat{X}^\dagger\hat{T}\hat{c}^\dagger_{\mathbf{k}+\mathbf{q}}\hat{c}_{\mathbf{k}}\hat{a}_{\mathbf{q}}, \hat{H}_{LO}]\rangle \\ =& G^*_{\mathbf{q}}\{N_X(1-N_T)(1+N_{\mathbf{q}})f_{\mathbf{k}+\mathbf{q}}(1-f_{\mathbf{k}}) \\ & -(1+N_X)N_TN_{\mathbf{q}}f_{\mathbf{k}}(1-f_{\mathbf{k}+\mathbf{q}})\}\end{aligned} \tag{15}$$

The formal integration of $\langle\hat{X}^\dagger\hat{T}\hat{c}^\dagger_{\mathbf{k}+\mathbf{q}}\hat{c}_{\mathbf{k}}\hat{a}_{\mathbf{q}}\rangle = \langle\hat{X}^\dagger\hat{T}\hat{c}^\dagger_{\mathbf{k}+\mathbf{q}}\hat{c}_{\mathbf{k}}\hat{a}_{\mathbf{q}}\rangle|_0 + \langle\hat{X}^\dagger\hat{T}\hat{c}^\dagger_{\mathbf{k}+\mathbf{q}}\hat{c}_{\mathbf{k}}\hat{a}_{\mathbf{q}}\rangle|_{LO}$, so we

have

$$\begin{aligned}
\langle \hat{X}^\dagger \hat{T} \hat{c}^\dagger_{\mathbf{k+q}} \hat{c}_{\mathbf{k}} \hat{a}_{\mathbf{q}} \rangle &= -\frac{iG^*_{\mathbf{q}}}{\hbar} \int_{-\infty}^{t} dt' e^{\frac{i}{\hbar}(E_X - E_T + \epsilon_{\mathbf{k+q}} - \epsilon_{\mathbf{k}} - \hbar\omega_0)(t-t')} \\
&\times \{N_X(1-N_T)(1+N_{\mathbf{q}}) f_{\mathbf{k+q}}(1-f_{\mathbf{k}}) - (1+N_X) N_T N_{\mathbf{q}} f_{\mathbf{k}}(1-f_{\mathbf{k+q}})\} \\
= &-\frac{iG^*_{\mathbf{q}}}{\hbar} (i\mathcal{P} \frac{1}{\frac{1}{\hbar}(E_X - E_T + \epsilon_{\mathbf{k+q}} - \epsilon_{\mathbf{k}} - \hbar\omega_0} + \pi\delta(\frac{1}{\hbar}(E_X - E_T + \epsilon_{\mathbf{k+q}} - \epsilon_{\mathbf{k}} - \hbar\omega_0)) \\
&\times \{N_X(1-N_T)(1+N_{\mathbf{q}}) f_{\mathbf{k+q}}(1-f_{\mathbf{k}}) - (1+N_X) N_T N_{\mathbf{q}} f_{\mathbf{k}}(1-f_{\mathbf{k+q}})\}
\end{aligned} \tag{16}$$

At last, we derive the Boltzmann equations that encompass phonon-assisted trion-exciton scattering processes.

$$\begin{aligned}
\frac{dN_T}{dt} = &-\frac{dN_X}{dt} = \frac{d}{dt}\langle \hat{T}^\dagger \hat{T} \rangle = \frac{1}{i\hbar}\langle [\hat{T}^\dagger \hat{T}, \hat{H}_0 + \hat{H}_{LO}] \rangle \\
&= \sum_{\mathbf{k},\mathbf{q}} \frac{2\pi |G_{\mathbf{q}}|^2}{\hbar} \delta(E_X - E_T + \epsilon_{\mathbf{k+q}} - \epsilon_{\mathbf{k}} - \hbar\omega_0) \\
&\quad \times \{N_X(1-N_T)(1+N_{\mathbf{q}}) f_{\mathbf{k+q}}(1-f_{\mathbf{k}}) - (1+N_X) N_T N_{\mathbf{q}} f_{\mathbf{k}}(1-f_{\mathbf{k+q}})\}
\end{aligned} \tag{17}$$

By defining the trion-exciton upconversion (Γ_{TX}) and downconversion (Γ_{XT}) rates which take into consideration the energy conservation and the Fermi-Dirac distribution of the particles

$$\begin{aligned}
\Gamma_{TX} &= \sum_{\mathbf{k},\mathbf{q}} \frac{2\pi |G_{\mathbf{q}}|^2}{\hbar} \delta(E_X - E_T + \epsilon_{\mathbf{k+q}} - \epsilon_{\mathbf{k}} - \hbar\omega_0) N_{\mathbf{q}} f_{\mathbf{k}}(1-f_{\mathbf{k+q}}) \\
\Gamma_{XT} &= \sum_{\mathbf{k},\mathbf{q}} \frac{2\pi |G_{\mathbf{q}}|^2}{\hbar} \delta(E_X - E_T + \epsilon_{\mathbf{k+q}} - \epsilon_{\mathbf{k}} - \hbar\omega_0)(1+N_{\mathbf{q}}) f_{\mathbf{k+q}}(1-f_{\mathbf{k}})
\end{aligned} \tag{18}$$

the Boltzmann equations, delineating the dynamics of trion and exciton populations at the same valley due to phonon scattering within a single valley, can be expressed as:

$$\begin{aligned}
\frac{dN_T}{dt} &= -\Gamma_{TX} N_T + \Gamma_{XT} N_X \\
\frac{dN_X}{dt} &= -\Gamma_{XT} N_X + \Gamma_{TX} N_T
\end{aligned} \tag{19}$$

Furthermore, incorporating the decay processes[35,48,49] and intervalley depolarization processes

between different valleys[8–11,50–54] for excitons and trions, we can express the comprehensive Boltzmann equations used for simulating the experimental data discussed in the main text, herein $\pm$ stands for the index of different valleys.

$$\begin{aligned}\frac{dN_{\pm,T}}{dt} &= -(\Gamma_{TX}+\Gamma_{TT}+\Gamma_{r,T})N_{\pm,T}+\Gamma_{XT}N_{\pm,X}+\Gamma_{TT}N_{\mp,T}\\ \frac{dN_{\pm,X}}{dt} &= -(\Gamma_{XT}+\Gamma_{XX}+\Gamma_{r,X})N_{\pm,X}+\Gamma_{TX}N_{\pm,T}+\Gamma_{XX}N_{\mp,X}\end{aligned} \tag{20}$$

In these equations above, Γ_{TX} and Γ_{XT} are calculated directly from Eqs. 11 and 18, based on results of trion and exciton binding energy and wavefunctions and the first-principles calculation results for el-ph couplings. $\Gamma_{r,X(T)}$ represents the decay rate of excitons (trions), $\Gamma_{XX(TT)}$ denotes the intervalley depolarization rate of excitons (trions). The parameters used in the simulation are fitted from the experimental results and are listed in the table below. These values are consistent with results in previous studies as shown in Table 2.[11,24,26,55–61]

Table S1: Parameters used in the Boltzmann equation

T (K)	Γ_{TX} (ps^{-1})	Γ_{XT} (ps^{-1})	Γ_{TT} (ps^{-1})	Γ_{XX} (ps^{-1})	$\Gamma_{r,T}$ (ps^{-1})	$\Gamma_{r,X}$ (ps^{-1})
290	3.54	0.45	0.30	15.0	0.05	0.05
180	1.41	0.23	0.30	10.0	0.05	0.05
78	0.09	0.08	0.10	5.0	0.05	0.05
12	0.00	0.01	0.10	1.0	0.05	0.05

The influence of trion complexes to the dynamic process

The trion complexes include the singlet and triplet trions, strictly speaking, it is more accurate to consider their scattering channels separately. When we focus on the scattering dynamics of the singlet and triplet trions (see $|+,T_s\rangle$ and $|+,T_{tr}\rangle$ as shown in Fig. S14) respectively, we observe that, for instance, when singlet trions in the K valley (see $|+,T_s\rangle$ in Fig. S14) are excited, they are mainly scattered to excitons in the same valley (K valley, see $|+,X\rangle$ in Fig. S14) by absorbing

Table S2: Parameters from references.

	Γ_{TT} (ps^{-1})	Γ_{XX} (ps^{-1})	$\Gamma_{r,T}$ (ps^{-1})	$\Gamma_{r,X}$ (ps^{-1})
MoS_2		5.0 (77 K)[27]		0.02 (300 K)[57]
$MoSe_2$	0.3 (20 K)[55]		0.06 (7 K)[58] 0.21 (20 K)[55] 0.08 (4 K)[62]	0.33 (4 K)[62] 0.004 (10 K)[63]
WS_2		4.76 (77 K)[56] 1.0 (4.5 K)[64]	0.01 (10 K)[60] 0.008 (5 K)[65]	0.26(5 K)[65] 0.01 (300 K)[66]
WSe_2	0.25 (13 K)[24] 0.08 (4 K)[59]	15.15 (300 K)[11] 0.17 (4 K)[67] 0.67 (125 K)[67]	0.05 (4 K)[59]	0.05 ($\sim$300 K)[26] 0.06 (10 K)[61]

phonons (relaxation process ① as shown in Fig. 1b of the main text) that satisfy the conservation of energy and momentum, or to triplet trions in the other valley (-K valley, see $|-, T_{tr}\rangle$ in Fig. S14) mainly due to the electron-hole exchange interaction (relaxation process ③ as shown in Fig. 1b of main text). Subsequently, the generated K valley excitons and -K valley triplet trions can experience intervalley depolarization and intravalley upconversion to evolve to the excitons in the -K valley (relaxation process ② and ④ as shown in Fig. 1b of the main text). Similar to the singlet trions in the K valley, when the triplet trions in the K valley are excited by pumping laser, they are mainly scattered to excitons in the same valley (K valley) or the singlet trions in the other valley (-K valley), followed by the scattering dynamics to the -K valley excitons. These two types of trion complexes will undergo similar dynamical processes that strongly depend on the chirality of related trions and excitons, allowing us to treat them as a unified entity.

Specifically, we made the approximation that triplet and singlet trions share a similar relaxation rate to exciton with assistance of phonons, $\Gamma_{Ttr,X} \sim \Gamma_{Ts,X} \sim \Gamma_{TX}$ where $\Gamma_{Ttr,X}$ and $\Gamma_{Ts,X}$ are the relaxation rate from to triplet and singlet trions to the exciton in the same valley respectively. Correspondingly, the down conversion rates are also assumed to be the same for triplet ($\Gamma_{X,Ttr}$) and singlet trions ($\Gamma_{X,Ts}$), $\Gamma_{X,Ttr} \sim \Gamma_{X,Ts} \sim \Gamma_{XT}$. These approximations shown above are reasonable to some extent since the trion wavefunction (Eqs. 7) of triplet and singlet trion only differs by

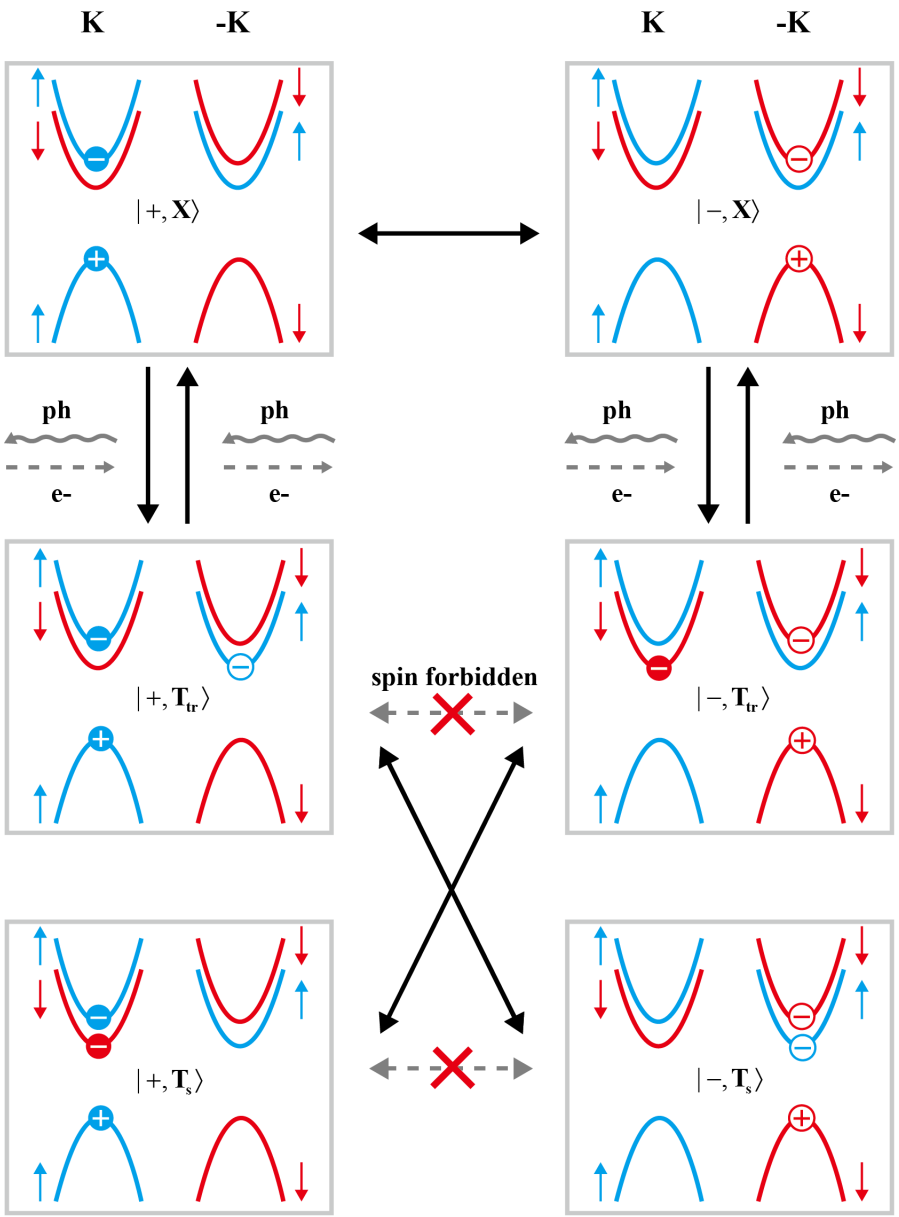

Figure S14: The diagram of scattering channels between bright exciton, spin singlet and triplet trion.

a phase term originating from the form factor and in the long-wave limit the form factor can be estimated to be close to 1. Consequently, in such approximations, the wavefunctions of singlet and triplet states of trions become similar. These results in some observable quantities being close in magnitude.

Furthermore, in the experiment, the difference of binding energies for these two trions is quite small ($\sim$ 7 meV),[9,68] which is comparable to the band widening of pumping laser (see Fig. S7). Thus, triplet and singlet trions are excited together in our pump-probe experiments. Additionally, due to the limitation of energy resolution, we cannot distinguish the difference of scattering channels for triplet and singlet trions at higher temperatures. For the simplification of the discussion, we combined them together.

The influence of dark excitons to the dynamic process

Numerous other potential scattering channels affect the population dynamics of excitons and trions, such as those through spin-forbidden dark excitons and trions. Previous studies have investigated the temperature-dependent photoluminescence and absorption in excitons and trions in tungsten- and molybdenum-based transition metal dichalcogenides (TMDs).[69,70] These studies reveal that, due to different spin configurations, the ordering of bright and dark states differs in the two types of TMDs, leading to varying temperature-dependent population ratios of bright and dark states. These lower-energy dark states in tungsten-based transition metal dichalcogenides will play a role in the steady-state photoluminescence. However, in time-resolved photoluminescence (TR-PL) experiments, some of the scattering processes involving the dark states may occur with much slower timescales than those considered in the Boltzmann equations or can be considered to pose the modification on the parameters used in the equations. We can analyze these dark states and the effects the dark states pose on the scattering dynamics one by one.

1. The intravalley spin-forbidden dark excitons consist of an electron and a hole in the same valley ($\mathbf{D_{X1}}$ in Fig. S15) but cannot be optically excited because this is a spin-flip transition. Consequently, they can couple to bright excitons and trions with a spin-flipping scattering

event, whose scattering rate is very small corresponding to a long scattering time. This process can be ignored in our simulations.

2. The dark trions with low energy ($\mathbf{D_T}$ in Fig. S15), however, consist of the two electrons from the lowest energy conduction band with opposite valley index and a hole, can couple to the singlet trions without flipping the spin.

3. The momentum-forbidden lowest energy dark excitons ($\mathbf{D_{X2}}$ in Fig. S15) can couple to bright excitons due to their identical spin alignment. Such scattering may be of the same order of the relaxation channels we considered.

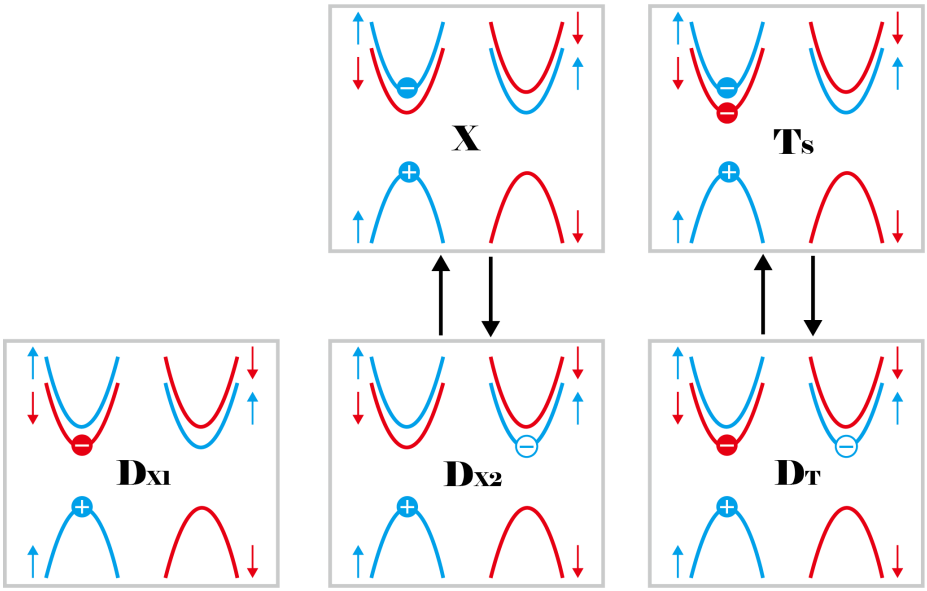

Figure S15: From left to right at the bottom are the lowest energy spin-forbidden dark exciton, momentum-forbidden dark exciton and the dark trion. The momentum-forbidden dark exciton and dark trion can couple to optical bright exciton and singlet trion without flipping the spin.

As shown above, the scattering channels involving dark trions and excitons can be considered as additional decay pathways for bright trions and excitons, having a similar influence to recombination processes for the sake of simplicity. Therefore, the contributions of these dark states are partly considered, which have been included in $\Gamma_{r,T}$ and $\Gamma_{r,X}$. Herein, $\Gamma_{r,T}$ and $\Gamma_{r,X}$ stand for decay rate of trions and excitons. Especially at the low temperature, we can see that these processes that involves absorbing phonons are suppressed. The excited trions can only depolarize to the other

valley or decay through emission, or to the low-energy dark states. The existence of the dark states at the low temperature merely enhances the decay rate of bright trions.

References

(1) Moody, G.; Schaibley, J.; Xu, X. Exciton dynamics in monolayer transition metal dichalcogenides. *JOSA B* **2016**, *33*, C39–C49.

(2) Jadczak, J.; Bryja, L.; Kutrowska-Girzycka, J.; Kapuściński, P.; Bieniek, M.; Huang, Y.-S.; Hawrylak, P. Room Temperature Multi-Phonon Upconversion Photoluminescence in Monolayer Semiconductor WS_2. *Nat. Commun.* **2019**, *10*, 107.

(3) Nagler, P.; Ballottin, M. V.; Mitioglu, A. A.; Durnev, M. V.; Taniguchi, T.; Watanabe, K.; Chernikov, A.; Schüller, C.; Glazov, M. M.; Christianen, P. C. M.; Korn, T. Zeeman Splitting and Inverted Polarization of Biexciton Emission in Monolayer WS_2. *Phys. Rev. Lett.* **2018**, *121*, 057402.

(4) Mai, C.; Barrette, A.; Yu, Y.; Semenov, Y. G.; Kim, K. W.; Cao, L.; Gundogdu, K. Many-Body Effects in Valleytronics: Direct Measurement of Valley Lifetimes in Single-Layer MoS_2. *Nano Lett.* **2014**, *14*, 202–206.

(5) Sayer, T.; Farah, Y. R.; Austin, R.; Sambur, J.; Krummel, A. T.; Montoya-Castillo, A. Trion formation resolves observed peak shifts in the optical spectra of transition-metal dichalcogenides. *Nano Lett.* **2023**, *23*, 6035–6041.

(6) Trovatello, C.; Katsch, F.; Li, Q.; Zhu, X.; Knorr, A.; Cerullo, G.; Dal Conte, S. Disentangling Many-body effects in the coherent optical response of 2D semiconductors. *Nano Lett.* **2022**, *22*, 5322–5329.

(7) Jones, A. M.; Yu, H.; Schaibley, J. R.; Yan, J.; Mandrus, D. G.; Taniguchi, T.; Watanabe, K.; Dery, H.; Yao, W.; Xu, X. Excitonic Luminescence Upconversion in a Two-Dimensional Semiconductor. **2016**, *12*, 323–327.

(8) Yu, T.; Wu, M. W. Valley depolarization due to intervalley and intravalley electron-hole exchange interactions in monolayer MoS_2. *Phys. Rev. B* **2014**, *89*, 205303.

(9) Yu, H.; Liu, G.-B.; Gong, P.; Xu, X.; Yao, W. Dirac cones and Dirac saddle points of bright excitons in monolayer transition metal dichalcogenides. *Nat. Commun.* **2014**, *5*, 3876.

(10) Lin, Z.; Liu, Y.; Wang, Z.; Xu, S.; Chen, S.; Duan, W.; Monserrat, B. Phonon-Limited Valley Polarization in Transition-Metal Dichalcogenides. *Phys. Rev. Lett.* **2022**, *129*, 027401.

(11) Chen, H.-Y.; Sangalli, D.; Bernardi, M. First-principles ultrafast exciton dynamics and time-domain spectroscopies: Dark-exciton mediated valley depolarization in monolayer WSe_2. *Phys. Rev. Res.* **2022**, *4*, 043203.

(12) Kormányos, A.; Burkard, G.; Gmitra, M.; Fabian, J.; Zólyomi, V.; Drummond, N. D.; Fal'ko, V. k· p theory for two-dimensional transition metal dichalcogenide semiconductors. *2D Mater.* **2015**, *2*, 022001.

(13) Xiao, D.; Liu, G.-B.; Feng, W.; Xu, X.; Yao, W. Coupled Spin and Valley Physics in Monolayers of MoS_2 and Other Group-VI Dichalcogenides. *Phys. Rev. Lett.* **2012**, *108*, 196802.

(14) Haug, H.; Koch, S. W. *Quantum theory of the optical and electronic properties of semiconductors*; World Scientific Publishing Company, 2009.

(15) Kresse, G.; Furthmüller, J. Efficient iterative schemes for ab initio total-energy calculations using a plane-wave basis set. *Phys. Rev. B* **1996**, *54*, 11169.

(16) Kresse, G.; Furthmüller, J. Efficiency of ab-initio total energy calculations for metals and semiconductors using a plane-wave basis set. *Comput. Mater. Sci.* **1996**, *6*, 15–50.

(17) Kresse, G.; Joubert, D. From ultrasoft pseudopotentials to the projector augmented-wave method. *Phys. Rev. B* **1999**, *59*, 1758.

(18) Zhang, D. K.; Kidd, D. W.; Varga, K. Excited Biexcitons in Transition Metal Dichalcogenides. *Nano Letters* **1996**, *15*, 7002–7005.

(19) Chandrasekhar, S. Some remarks on the negative hydrogen ion and its absorption coefficient. *Astrophys. J.* **1944**, *100*, 176–180.

(20) Sergeev, R. A.; Suris, R. A. Ground-State Energy of X and X+ Trions in a Two-Dimensional Quantum Well at an Arbitrary Mass Ratio. *Physics of the Solid State* **2001**, *43*, 746–751.

(21) Sergeev, R.; Suris, R.; Astakhov, G.; Ossau, W.; Yakovlev, D. Universal estimation of X-trion binding energy in semiconductor quantum wells. *The European Physical Journal B-Condensed Matter and Complex Systems* **2005**, *47*, 541–547.

(22) Giannozzi, P.; Baroni, S.; Bonini, N.; Calandra, M.; Car, R.; Cavazzoni, C.; Ceresoli, D.; Chiarotti, G. L.; Cococcioni, M.; Dabo, I., et al. QUANTUM ESPRESSO: a modular and open-source software project for quantum simulations of materials. *Journal of physics: Condensed matter* **2009**, *21*, 395502.

(23) Noffsinger, J.; Giustino, F.; Malone, B. D.; Park, C.-H.; Louie, S. G.; Cohen, M. L. EPW: A program for calculating the electron–phonon coupling using maximally localized Wannier functions. *Comput. Phys. Commun.* **2010**, *181*, 2140–2148.

(24) Singh, A.; Tran, K.; Kolarczik, M.; Seifert, J.; Wang, Y.; Hao, K.; Pleskot, D.; Gabor, N. M.; Helmrich, S.; Owschimikow, N., et al. Long-lived valley polarization of intravalley trions in monolayer WSe_2. *Phys. Rev. Lett.* **2016**, *117*, 257402.

(25) Hao, K.; Xu, L.; Wu, F.; Nagler, P.; Tran, K.; Ma, X.; Schüller, C.; Korn, T.; MacDonald, A. H.; Moody, G., et al. Trion valley coherence in monolayer semiconductors. *2D Mater.* **2017**, *4*, 025105.

(26) Cui, Q.; Ceballos, F.; Kumar, N.; Zhao, H. Transient absorption microscopy of monolayer and bulk WSe_2. *ACS nano* **2014**, *8*, 2970–2976.

(27) Dal Conte, S.; Bottegoni, F.; Pogna, E. A. A.; De Fazio, D.; Ambrogio, S.; Bargigia, I.; D'Andrea, C.; Lombardo, A.; Bruna, M.; Ciccacci, F.; Ferrari, A. C.; Cerullo, G.; Finazzi, M. Ultrafast valley relaxation dynamics in monolayer MoS_2 probed by nonequilibrium optical techniques. *Phys. Rev. B* **2015**, *92*, 235425.

(28) Moody, G.; Kavir Dass, C.; Hao, K.; Chen, C.-H.; Li, L.-J.; Singh, A.; Tran, K.; Clark, G.; Xu, X.; Berghäuser, G.; Malic, E.; Knorr, A.; Li, X. Intrinsic Homogeneous Linewidth and Broadening Mechanisms of Excitons in Monolayer Transition Metal Dichalcogenides. *Nature Communications* **2015**, *6*, 8315.

(29) Wang, H.; Zhang, C.; Rana, F. Surface Recombination Limited Lifetimes of Photoexcited Carriers in Few-Layer Transition Metal Dichalcogenide MoS $_2$. *Nano Letters* **2015**, *15*, 8204–8210.

(30) Wang, Z.; Molina-Sánchez, A.; Altmann, P.; Sangalli, D.; De Fazio, D.; Soavi, G.; Sassi, U.; Bottegoni, F.; Ciccacci, F.; Finazzi, M.; Wirtz, L.; Ferrari, A. C.; Marini, A.; Cerullo, G.; Dal Conte, S. Intravalley Spin–Flip Relaxation Dynamics in Single-Layer WS $_2$. *Nano Letters* **2018**, *18*, 6882–6891.

(31) Rohlfing, M.; Louie, S. G. Electron-hole excitations and optical spectra from first principles. *Phys. Rev. B* **2000**, *62*, 4927–4944.

(32) Onida, G.; Reining, L.; Rubio, A. Electronic excitations: density-functional versus many-body Green's-function approaches. *Rev. Mod. Phys.* **2002**, *74*, 601–659.

(33) Qiu, D. Y.; da Jornada, F. H.; Louie, S. G. Optical Spectrum of MoS_2: Many-Body Effects and Diversity of Exciton States. *Phys. Rev. Lett.* **2013**, *111*, 216805.

(34) Zhang, C.; Wang, H.; Chan, W.; Manolatou, C.; Rana, F. Absorption of light by excitons and trions in monolayers of metal dichalcogenide MoS_2: Experiments and theory. *Phys. Rev. B* **2014**, *89*, 205436.

(35) Wang, H.; Zhang, C.; Chan, W.; Manolatou, C.; Tiwari, S.; Rana, F. Radiative lifetimes of excitons and trions in monolayers of the metal dichalcogenide MoS_2. *Phys. Rev. B* **2016**, *93*, 045407.

(36) Keldysh, L. Coulomb interaction in thin semiconductor and semimetal films. *Soviet Journal of Experimental and Theoretical Physics Letters* **1979**, *29*, 658.

(37) Chernikov, A.; Berkelbach, T. C.; Hill, H. M.; Rigosi, A.; Li, Y.; Aslan, B.; Reichman, D. R.; Hybertsen, M. S.; Heinz, T. F. Exciton binding energy and nonhydrogenic Rydberg series in monolayer WS_2. *Phys. Rev. Lett.* **2014**, *113*, 076802.

(38) Mostaani, E.; Szyniszewski, M.; Price, C. H.; Maezono, R.; Danovich, M.; Hunt, R. J.; Drummond, N. D.; Fal'ko, V. I. Diffusion quantum Monte Carlo study of excitonic complexes in two-dimensional transition-metal dichalcogenides. *Phys. Rev. B* **2017**, *96*, 075431.

(39) Berkelbach, T. C.; Hybertsen, M. S.; Reichman, D. R. Theory of neutral and charged excitons in monolayer transition metal dichalcogenides. *Phys. Rev. B* **2013**, *88*, 045318.

(40) Sergeev, R.; Suris, R. Ground-state energy of X- and X+ trions in a two-dimensional quantum well at an arbitrary mass ratio. *Phys. Solid State* **2001**, *43*, 746–751.

(41) Szyniszewski, M.; Mostaani, E.; Drummond, N. D.; Fal'Ko, V. Binding energies of trions and biexcitons in two-dimensional semiconductors from diffusion quantum Monte Carlo calculations. *Phys. Rev. B* **2017**, *95*, 081301.

(42) Mayers, M. Z.; Berkelbach, T. C.; Hybertsen, M. S.; Reichman, D. R. Binding energies and spatial structures of small carrier complexes in monolayer transition-metal dichalcogenides via diffusion Monte Carlo. *Phys. Rev. B* **2015**, *92*, 161404.

(43) Giannozzi, P.; Andreussi, O.; Brumme, T.; Bunau, O.; Nardelli, M. B.; Calandra, M.; Car, R.; Cavazzoni, C.; Ceresoli, D.; Cococcioni, M., et al. Advanced capabilities for materials modelling with Quantum ESPRESSO. *Journal of physics: Condensed matter* **2017**, *29*, 465901.

(44) Kaasbjerg, K.; Thygesen, K. S.; Jacobsen, K. W. Phonon-limited mobility in n-type single-layer MoS_2 from first principles. *Phys. Rev. B* **2012**, *85*, 115317.

(45) Gunst, T.; Markussen, T.; Stokbro, K.; Brandbyge, M. First-principles method for electron-phonon coupling and electron mobility: Applications to two-dimensional materials. *Phys. Rev. B* **2016**, *93*, 035414.

(46) Mahan, G. D. *Many-particle physics*; Springer Science & Business Media, 2000.

(47) Selig, M.; Berghäuser, G.; Raja, A.; Nagler, P.; Schüller, C.; Heinz, T. F.; Korn, T.; Chernikov, A.; Malic, E.; Knorr, A. Excitonic linewidth and coherence lifetime in monolayer transition metal dichalcogenides. *Nat. Commun.* **2016**, *7*, 13279.

(48) Korn, T.; Heydrich, S.; Hirmer, M.; Schmutzler, J.; Schüller, C. Low-temperature photocarrier dynamics in monolayer MoS_2. *Appl. Phys. Lett.* **2011**, *99*.

(49) Pöllmann, C.; Steinleitner, P.; Leierseder, U.; Nagler, P.; Plechinger, G.; Porer, M.; Bratschitsch, R.; Schüller, C.; Korn, T.; Huber, R. Resonant internal quantum transitions and femtosecond radiative decay of excitons in monolayer WSe_2. *Nature Mater.* **2015**, *14*, 889–893.

(50) Mai, C.; Barrette, A.; Yu, Y.; Semenov, Y. G.; Kim, K. W.; Cao, L.; Gundogdu, K. Many-body effects in valleytronics: direct measurement of valley lifetimes in single-layer MoS_2. *Nano Lett.* **2014**, *14*, 202–206.

(51) Schmidt, R.; Berghauser, G.; Schneider, R.; Selig, M.; Tonndorf, P.; Malic, E.; Knorr, A.; Michaelis de Vasconcellos, S.; Bratschitsch, R. Ultrafast coulomb-induced intervalley coupling in atomically thin WS_2. *Nano Lett.* **2016**, *16*, 2945–2950.

(52) Mahmood, F.; Alpichshev, Z.; Lee, Y.-H.; Kong, J.; Gedik, N. Observation of exciton–exciton interaction mediated valley depolarization in monolayer $MoSe_2$. *Nano Lett.* **2018**, *18*, 223–228.

(53) Katsch, F.; Selig, M.; Knorr, A. Exciton-scattering-induced dephasing in two-dimensional semiconductors. *Phys. Rev. Lett.* **2020**, *124*, 257402.

(54) Kunin, A.; Chernov, S.; Bakalis, J.; Li, Z.; Cheng, S.; Withers, Z. H.; White, M. G.; Schönhense, G.; Du, X.; Kawakami, R. K., et al. Momentum-Resolved Exciton Coupling and Valley Polarization Dynamics in Monolayer WS_2. *Phys. Rev. Lett.* **2023**, *130*, 046202.

(55) Hao, K.; Xu, L.; Wu, F.; Nagler, P.; Tran, K.; Ma, X.; Schüller, C.; Korn, T.; MacDonald, A. H.; Moody, G.; Li, X. Trion Valley Coherence in Monolayer Semiconductors. *2D Mater.* **2017**, *4*, 025105.

(56) Wang, Z.; Molina-Sanchez, A.; Altmann, P.; Sangalli, D.; De Fazio, D.; Soavi, G.; Sassi, U.; Bottegoni, F.; Ciccacci, F.; Finazzi, M., et al. Intravalley spin–flip relaxation dynamics in single-layer WS_2. *Nano Lett.* **2018**, *18*, 6882–6891.

(57) Wang, H.; Zhang, C.; Rana, F. Surface recombination limited lifetimes of photoexcited carriers in few-layer transition metal dichalcogenide MoS_2. *Nano Lett.* **2015**, *15*, 8204–8210.

(58) Robert, C.; Lagarde, D.; Cadiz, F.; Wang, G.; Lassagne, B.; Amand, T.; Balocchi, A.; Renucci, P.; Tongay, S.; Urbaszek, B.; Marie, X. Exciton radiative lifetime in transition metal dichalcogenide monolayers. *Phys. Rev. B* **2016**, *93*, 205423.

(59) Wang, G.; Bouet, L.; Lagarde, D.; Vidal, M.; Balocchi, A.; Amand, T.; Marie, X.; Urbaszek, B. Valley dynamics probed through charged and neutral exciton emission in monolayer WSe_2. *Phys. Rev. B* **2014**, *90*, 075413.

(60) Zhao, J.; Zhao, W.; Du, W.; Su, R.; Xiong, Q. Dynamics of Exciton Energy Renormalization in Monolayer Transition Metal Disulfides. *Nano Res.* **2020**, *13*, 1399–1405.

(61) Moody, G.; Kavir Dass, C.; Hao, K.; Chen, C.-H.; Li, L.-J.; Singh, A.; Tran, K.; Clark, G.; Xu, X.; Berghäuser, G., et al. Intrinsic homogeneous linewidth and broadening mechanisms of excitons in monolayer transition metal dichalcogenides. *Nat. Commun.* **2015**, *6*, 8315.

(62) Wang, G.; Palleau, E.; Amand, T.; Tongay, S.; Marie, X.; Urbaszek, B. Polarization and

Time-Resolved Photoluminescence Spectroscopy of Excitons in $MoSe_2$ Monolayers. *Appl. Phys. Lett.* **2015**, *106*, 112101.

(63) Gao, F.; Gong, Y.; Titze, M.; Almeida, R.; Ajayan, P. M.; Li, H. Valley trion dynamics in monolayer $MoSe_2$. *Phys. Rev. B* **2016**, *94*, 245413.

(64) Plechinger, G.; Nagler, P.; Arora, A.; Schmidt, R.; Chernikov, A.; Del Águila, A. G.; Christianen, P. C.; Bratschitsch, R.; Schüller, C.; Korn, T. Trion fine structure and coupled spin–valley dynamics in monolayer tungsten disulfide. *Nat. Commun.* **2016**, *7*, 12715.

(65) Wang, A.; Wang, Y.; Li, J.; Xu, N.; Li, S.; Wang, X.; Shi, Y.; Wang, F. Controlling Relaxation Dynamics of Excitonic States in Monolayer Transition Metal Dichalcogenides WS_2 through Interface Engineering. *Appl. Phys. Lett.* **2021**, *118*, 121104.

(66) Fu, Y.; He, D.; He, J.; Bian, A.; Zhang, L.; Liu, S.; Wang, Y.; Zhao, H. Effect of dielectric environment on excitonic dynamics in monolayer WS_2. *Adv. Mater. Interfaces* **2019**, *6*, 1901307.

(67) Zhu, C. R.; Zhang, K.; Glazov, M.; Urbaszek, B.; Amand, T.; Ji, Z. W.; Liu, B. L.; Marie, X. Exciton Valley Dynamics Probed by Kerr Rotation in WSe_2 Monolayers. *Phys. Rev. B* **2014**, *90*, 161302.

(68) Yu, H.; Cui, X.; Xu, X.; Yao, W. Valley excitons in two-dimensional semiconductors. *National Science Review* **2015**, *2*, 57–70.

(69) Arora, A.; Wessling, N. K.; Deilmann, T.; Reichenauer, T.; Steeger, P.; Kossacki, P.; Potemski, M.; Michaelis de Vasconcellos, S.; Rohlfing, M.; Bratschitsch, R. Dark trions govern the temperature-dependent optical absorption and emission of doped atomically thin semiconductors. *Phys. Rev. B* **2020**, *101*, 241413.

(70) Zhang, X.-X.; You, Y.; Zhao, S. Y. F.; Heinz, T. F. Experimental Evidence for Dark Excitons in Monolayer WSe_2. *Phys. Rev. Lett.* **2015**, *115*, 257403.